SURFACE IMPEDANCE INTEGRAL EQUATIONS FOR QUASISTATIONARY FIELD ANALYSIS IN AXI-SYMMECTRIC SYSTEMS

by

K.D. Himal C. Jayatilaka

A Thesis
Submitted to the Faculty of Graduate Studies
In Partial Fulfilment of the Requirements
For the Degree of
Master of Science

Department of Electrical and Computer Engineering
University of Manitoba,
Winnipeg, Canada

SURFACE IMPEDANCE INTEGRAL EQUATIONS FOR QUASISTATIONARY FIELD ANALYSIS IN AXISYMMECTRIC SYSTEMS

by

K.D. Himal C. Jayatilaka

A Thesis
Submitted to the Faculty of Graduate Studies
In Partial Fulfilmant of the Requirements
For the Degree of
Master of Science

Department of Electrical and Computer Engineering
University of Manitoba,
Winnipeg, Canada

THE UNIVERSITY OF MANITOBA

FACULTY OF GRADUATE STUDIES

*****

COPYRIGHT PERMISSION

SURFACE IMPEDANCE INTEGRAL EQUATIONS FOR QUASISTATIONARY FIELD ANALYSIS IN AXISYMMECTRIC SYSTEMS

BY

K. D. Himal C. Jayatilaka

A Thesis/Practicum submitted to the Faculty of Graduate Studies of The University of Manitoba in partial fulfillment of the requirement of the degree

Of

MASTER OF SCIENCE

To my parents.

Acknowledgements

I would like to express deep gratitude to my advisor, Professor Ioan R. Ciric for his invaluable guidance, support, encouragement and insight throughout my research. I wish to thank my examining committee members for their help and criticism. I wish to acknowledge the financial support from The University of Manitoba in the form of a University Fellowship. I would like to thank Mr. N. Jayasekara for providing numerical data from exact analytical models.

Finally, I am grateful to my parents and my sister for their guidance and continuous support that has helped me in completing this degree and achieving my goals in life.

Abstract

Surface integral equations satisfied by the induced current density are formulated for axisymmetric solid conductors by applying the surface impedance model and the perfect conductor model. Their performance is investigated employing spheres and, also, prolate and oblate conducting spheroids with a large range of geometric parameters at different frequencies. Surface integral equations are also formulated using the modified surface impedance with first order curvature correction.

Integral equations are solved by applying a well known numerical technique, namely the method of moments. Different expansion functions and different weighting functions are employed to improve the accuracy. Numerical results generated are compared with available analytical results and with experimental data. The effects of employing different surface discretizations are presented. The range of validity of the surface impedance integral equations is also investigated.

Table of Contents

Appendices

List of Tables

List of Figures

List of Symbols

$\boldsymbol{A}$ - Magnetic vector potential

$\boldsymbol{B}$ - Magnetic flux density

$\boldsymbol{D}$ - Electric flux density

$\boldsymbol{E}$ - Electric field intensity

F - Force

$f_m(t)$ - Basis function

$\boldsymbol{H}$ - Magnetic field intensity

I - Electric current

$\boldsymbol{J}$ - Electric current density

k - Wave number

P - Power loss

$\boldsymbol{r}$ - Position vector of the observation point

$\boldsymbol{r}$' - Position vector of a source point

$\boldsymbol{R}$ - Distance vector from a source point to the observation point

r, θ, ϕ - Sperical coordinates

$w_n(t)$ - Weighting function

Z_s - Standard surface impedance

Z_{smod} - Modified surface impedance

δ - Depth of penetration

ϵ - Permittivity of the media

η, ξ, ϕ - Prolate and oblate coordinates

μ - Permeability of the media

μ_0 - Permeability of free space ($10^{-9}/36\pi$ H/m)

ρ - Electric charge density

ρ, ϕ, z - Cylindrical coordinates

σ - Conductivity

Chapter 1

Introduction

1.1 Overview and Objective

The behavior of electromagnetic fields is completely described by Maxwell's equations and the associated boundary conditions. Solving electromagnetic field problems using exact analytical methods is impossible for most engineering applications. Many numerical methods, in both the time and frequency domains, have been developed for the analysis of engineering electromagnetic problems. The method of moments (MoM) has become one of the most important numerical methods using the integral equation approach in computational electromagnetics.

In the MoM, a functional operator equation describing the physical problem is transformed into a matrix equation by, first, approximating the unknown functions using a set of expansion functions with a set of unknown coefficients and, then, performing a scalar product of the operator equation with selected testing functions [5]. The MoM has been enriched by many researchers and new features have been added over the last three decades. In this thesis, MoM is applied to the quasistationary field analysis.

Kirchhoff developed an integral representation of electromagnetic fields in terms of field producing sources, which are volume and surface distribution of current and charges [15]. An integral equation is formed by applying relevant boundary conditions, via the Kirchhoff

integral representation. When the unknowns are volume source distributions the associated integral equation is called a volume integral equation, whereas when the unknowns are surface source distributions or equivalent surface distributions the associated integral equation is called a surface integral equation (or boundary integral equation) [11] [12]. In wave scattering problems, a volume integral equation is formed by replacing obstacles with free space and equivalent sources. In many cases, scattering problems are modelled by a boundary integral equations in terms of electric and magnetic currents if the scatterer is homogeneous [8]. The integral equation is converted into a matrix equation by applying MoM.

Boundary integral equations are used for solving a wide range of electromagnetic field problems. They have the advantage of requiring less computation than methods based on the discretization of the entire conducting region. In general, the accuracy of solutions of these integral equations is higher than that of solutions of corresponding differential equations. This is due to the fact that errors at various points may partially cancel each other in the summation process of the integral methods, whereas, in general, errors propagate along successive steps when using numerical differential methods. The perfect conductor (PC) model is commonly used in the formulation of surface integral equations for solid conductors at high frequencies. It is a reasonable approximation because at high frequencies electromagnetic fields confine to the outer surface of good conductors. The validity of this model has been analyzed in [1] for spheroids of various axial ratios by comparing analytical results with experimental data. At lower frequencies, the electromagnetic field penetrates into conductors and the PC model is not a good approximation. The standard surface impedance (SI) model is used at lower frequencies in the formulation of various finite element [9] and boundary integral equation [14] techniques. The available literature about the application of the SI model to integral equation formulations is sparce, specially at low frequencies (as in eddy current problems,

etc..). On the other hand, there are many references dealing with the application of the SI impedance model at higher frequencies (as in wave scattering problems, etc..). Leontovich and others have modified the surface impedance introducing a first order curvature correction and Mitzner [10] has corrected it.

In this thesis, surface integral equations for axisymmetric conductors in the presence of quasistationary magnetic fields are formulated using both the SI and PC models. These integral equations are useful in certain applications such as induction heating, heat treatment, electromagnetic levitation and other eddy current problems. The integral equations are solved numerically for the unknown current density by applying different expansion functions and weighting functions in order to analyze their accuracy. Power losses and electromagnetic forces are derived from the induced current determined from SI and PC integral equations, and are compared with available analytical results and with measured data for various conducting spheres, and prolate and oblate spheroids in the presence of magnetic field produced by current-carrying turns. Numerical results obtained from the modified surface impedance (MSI) integral equation are compared with those determined from the SI integral equation. The minimum number of necessary unknowns for a desired accuracy is also determined for the spherical and spheroidal conductors. The range of validity of the SI integral equations is also investigated.

1.2 Thesis Outline

Chapter 2 describes theoretical aspects which are useful in the formulation of integral equations. Electromagnetic fields are represented in integral forms and their evolutions are given starting from Maxwell's equations.The SI model is derived using the phenomena of incidence of plane waves on an conducting semispace. A mathematical explanation for MOM is also

presented.

In chapter 3, the formulation of integral equations for arbitrary shaped conductors is presented. They are solved applying a point matching procedure. A convenient way of defining the surface of the arbitrary shaped conductors is given. The integrals involved are taken in principal values and the evaluation of their singularities is elaborated. The electromagnetic force upon conducting bodies is evaluated in a simple manner. Chapter 3 also explains the calculation of power loss in conducting bodies numerically.

Chapter 4 is dedicated to formulate integral equations for spherical conductors in the presence of magnetic fields produced by current-carrying turns. Formulas are derived in spherical coordinates to numerically evaluate quasistationary electromagnetic fields created by a single current-carrying turn. The SI and PC integral equations are solved applying the point matching procedure. The power losses and electromagnetic forces are evaluated at different frequencies from both the SI and PC models for spherical conductors with different ratio of sphere radius to the depth of penetration and compared with exact analytical solutions. The range of validity of the results from the SI integral equations is also investigated using spherical conductors in chapter 4. The accuracy of the results is improved by employing a finer mesh. Galerkin's method is also implemented using three constrained rectangular pulse functions.

Integral equations formulated in spheroidal coordinates are given in Chapter 5. An introduction to the prolate coordinate system is presented at the outset of the chapter. It is convenient to use the prolate coordinate system in the formulation of integral equations for prolate spheroidal conductors because tangential field components can be found easily. Power loss and force are evaluated using the point matching and the Galerkin method for prolate

spheroidal conductors with different axial ratios and compared with corresponding analytical results and available experimental data. Numerical results evaluated from MSI integral equations are also presented.

In Chapter 6, the oblate coordinate system is used to formulate integral equations. Power loss and force are evaluated for a wide range of oblate spheroidal conductors from the SI and PC integral equations and compared with relevant analytical results. Chapter 7 contains conclusions and suggestions for future work.

Chapter 2

Background Theory

In this chapter, the representation of electromagnetic fields in the integral form is discussed starting from Maxwell equations. The concept of the magnetic vector potential is used in the representation of electric field in integral form. Quasistationary electric and magnetic fields produced by a current-carrying turn in free space are given both in the form of integrals and as summations, which are used to calculate the fields numerically. The surface impedance and the skin depth are described at the end of this chapter. The modification of the surface impedance for smooth boundaries is also explained.

2.1 Integral Representation of Electromagnetic Fields

Electromagnetic field quantities, whenever they have continuous derivatives, obey Maxwell equations, which in the frequency domain are

$$\nabla \times \boldsymbol{H} = j\omega \boldsymbol{D} + \boldsymbol{J} \tag{2.1}$$

$$\nabla \times \boldsymbol{E} = -j\omega \boldsymbol{B} \tag{2.2}$$

$$\nabla \cdot \boldsymbol{D} = \rho \tag{2.3}$$

$$\nabla \cdot \boldsymbol{B} = 0 \tag{2.4}$$

where $\boldsymbol{E}$ is the electric field intensity, $\boldsymbol{H}$ is the magnetic field intensity , $\boldsymbol{J}$ and ρ are the electric current density and the electric charge density respectively, and ω is the angular frequency. The field intensities $\boldsymbol{E}$ and $\boldsymbol{H}$ are related to the electric flux density $\boldsymbol{D}$ and magnetic flux density $\boldsymbol{B}$ as

$$\boldsymbol{D} = \epsilon \boldsymbol{E} \tag{2.5}$$

$$\boldsymbol{B} = \mu \boldsymbol{H} \tag{2.6}$$

where ϵ and μ are the permittivity and the permeability of the linear isotropic media.

It is a well known vector identity that the divergence of a vector which is itself the curl of another vector is zero and so satisfies (2.4). Helmholtz theorem states that a vector is uniquely defined if, and only if, both its curl and its divergence are specified. Thus, we can define a new vector $\boldsymbol{A}$ which we call the magnetic vector potential as a vector whose divergence is zero and whose curl is $\boldsymbol{B}$,

$$\nabla \times \boldsymbol{A} = \boldsymbol{B} \qquad\qquad \nabla \cdot \boldsymbol{A} = 0. \tag{2.7}$$

Substitution of (2.7) into (2.2) yields an expression for $\boldsymbol{E}$ in terms of $\boldsymbol{A}$ and of a scalar potential ϕ,

$$\boldsymbol{E} = -j\omega \boldsymbol{A} - \nabla \phi. \tag{2.8}$$

In some eddy-current problems, only the induced component of $\boldsymbol{E}$ is of practical importance, *i.e.*

$$\boldsymbol{E} = -j\omega \boldsymbol{A}. \tag{2.9}$$

Displacement current $j\omega \boldsymbol{D}$ is negligible as compared with $\boldsymbol{J}$ for quasistationary fields. In

regions with uniform permeability , (2.1) is written as

$$\nabla \times \boldsymbol{B} = \mu \boldsymbol{J}. \tag{2.10}$$

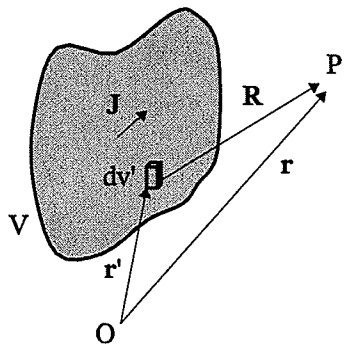

Figure 2.1: Volume current distribution.

With the vector identity $\nabla \times (\nabla \times \boldsymbol{A}) = \nabla(\nabla \cdot \boldsymbol{A}) - (\nabla \cdot \nabla)\boldsymbol{A}$ and equation (2.7), (2.10) yields $\nabla^2 \boldsymbol{A} = \mu \boldsymbol{J}$. For an unbounded homogeneous space, the well known solution of this equation is [13]

$$\boldsymbol{A}(r) = \frac{\mu}{4\pi} \int_V \frac{\boldsymbol{J}(\mathrm{r})dv'}{R} \tag{2.11}$$

where $\boldsymbol{R} = \boldsymbol{r} - \boldsymbol{r}'$, $\boldsymbol{r}$, $\boldsymbol{r}'$ being the position vectors of the observation point P and the source point, respectively, and dv' being the volume element. The volume current density is constrained in a finite volume V, as shown in Fig. 2.1. A surface current density $\boldsymbol{J}_S$ on a surface S in a homogeneous unbounded space produces

$$\boldsymbol{A}(r) = \frac{\mu}{4\pi} \int_S \frac{\boldsymbol{J}_s(r')ds'}{R} \tag{2.12}$$

where ds' is the surface element on S, as shown in Fig. 2.2. In a similar manner, the vector potential in an unbounded homogeneous space produced by a wire carrying a current I is given by

$$\boldsymbol{A}(r) = \frac{\mu I}{4\pi} \int_C \frac{d\boldsymbol{l}'}{R} \tag{2.13}$$

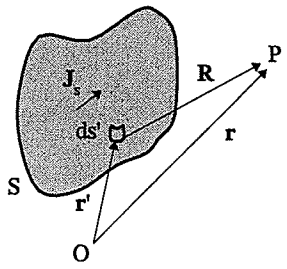

Figure 2.2: Surface current distribution.

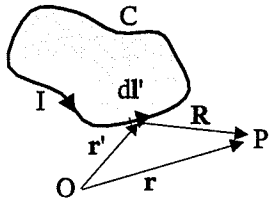

Figure 2.3: Line current.

where $d\boldsymbol{l}'$ is a vector length element in the direction of the current along the wire, as depicted in Fig. 2.3. Taking the curl of both sides of (2.13), we have the relation

$$\boldsymbol{B}(\boldsymbol{r}) = \frac{\mu I}{4\pi} \int_C \frac{d\boldsymbol{l}' \times \boldsymbol{R}}{R^3} \tag{2.14}$$

Similarly, the expression for $\boldsymbol{B}$ in terms of $\boldsymbol{J}_s$ is

$$\boldsymbol{B}(\boldsymbol{r}) = \frac{\mu}{4\pi} \int_S \frac{\boldsymbol{J}_s(\boldsymbol{r}') \times \boldsymbol{R}}{R^3} ds'. \tag{2.15}$$

2.1.1 Induced Electric Field due to a Single Current-Carrying Turn

In this section, the electric field produced by a single current-carrying turn in free space is obtained since it is needed in the solution method by integral equations in chapter 3. The circular turn has a radius b_s and is located in a plane $z = z_s$. Rectangular and cylindrical

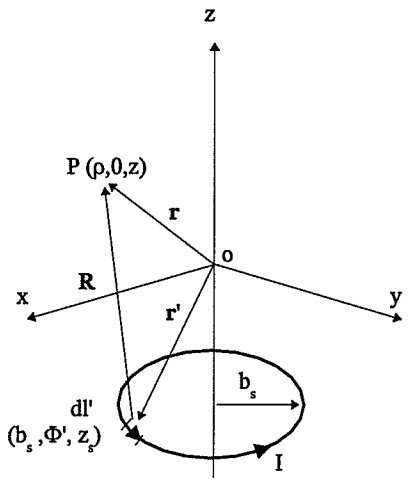

Figure 2.4: Current-carrying turn in free space.

coordinate systems are used in the solution method. From symmetry, it is known that in cylindrical coordinates the vector potential $\boldsymbol{A}$ has only a component A_ϕ in the azimuthal ϕ-direction and its magnitude is independent of ϕ. Therefore, for simplicity, the point P is chosen in the semispace $\phi = 0$, x and z coordinates of P being ρ and z respectively.

The position vectors $\boldsymbol{r}$ and $\boldsymbol{r'}$ are expressed as $\rho \boldsymbol{u}_x + z\boldsymbol{u}_z$ and $b_s \cos\phi' \boldsymbol{u}_x + b_s \sin\phi' \boldsymbol{u}_y + z_s \boldsymbol{u}_z$, respectively, where $\boldsymbol{u}_x$, $\boldsymbol{u}_y$ and $\boldsymbol{u}_z$ are unit vectors in x, y and z directions and the vector length element is $d\boldsymbol{l'}$. Then

$$R = |\boldsymbol{r} - \boldsymbol{r'}| = \sqrt{(\rho - b_s \cos\phi')^2 + b_s^2 \sin^2\phi' + (z - z_s)^2}$$

Substituting $d\boldsymbol{l'}$ and R in (2.13), we have

$$A_\phi = \frac{\mu_0 I}{4\pi} \int_0^{2\pi} \frac{b_s \cos\phi' d\phi'}{\sqrt{\rho^2 + b_s^2 - 2\rho b_s \cos\phi' + (z - z_s)^2}}. \tag{2.16}$$

This integral has to be solved numerically. The turn is divided into a number of L elements and R is considered to be the distance from the center of elements to the point P. Equation

(2.16) is expressed as

$$A_\phi = \frac{\mu_0 I}{4\pi} \sum_{i=1}^{L} \frac{b_s \cos\{\frac{2\pi}{L}(i-1)\}\frac{2\pi}{L}}{\sqrt{\rho^2 + b_s^2 - 2\rho b_s \cos\{\frac{2\pi}{L}(i-1)\} + (z-z_s)^2}} \tag{2.17}$$

As shown earlier, the electric field intensity is related to $\boldsymbol{A}$ by (2.9). Since $\boldsymbol{A}$ has only a component in azimuthal ϕ-direction, $\boldsymbol{E}$ has also only a component E_ϕ in ϕ-direction. Then, from (2.17) and (2.9) we obtain

$$E_\phi = -\frac{j\omega\mu_0 I}{4\pi} \sum_{i=1}^{L} \frac{b_s \cos\{\frac{2\pi}{L}(i-1)\}\frac{2\pi}{L}}{\sqrt{\rho^2 + b_s^2 - 2\rho b_s \cos\{\frac{2\pi}{L}(i-1)\} + (z-z_s)^2}}. \tag{2.18}$$

The electric field intensity ΔE_ϕ at P produced by a narrow circular strip having a uniform surface current of density $\boldsymbol{J}_s$ can be obtained from (2.18) by assuming that all the current is concentrated on the center line of the strip. For a circular strip of width $\triangle w$ located such that its center line is coincident with the current carrying turn in Fig. 2.4, we have

$$\Delta E_\phi = -\frac{j\omega\mu_0 J_s \triangle w}{4\pi} \sum_{i=1}^{L} \frac{b_s \cos\{\frac{2\pi}{L}(i-1)\}\frac{2\pi}{L}}{\sqrt{\rho^2 + b_s^2 - 2\rho b_s \cos\{\frac{2\pi}{L}(i-1)\} + (z-z_s)^2}}. \tag{2.19}$$

2.1.2 Magnetic Field due to a Single Current-Carrying Turn

The magnetic field produced by a circular current-carrying turn in free space is also needed in the formulation of SI and MSI integral equations for axisymmetric systems. Equation (2.14) developed in section 2.1 is used to compute the quasistationary magnetic flux density at P. With $d\boldsymbol{l}' = -b_s d\phi' \sin\phi' \boldsymbol{u}_x + b_s d\phi' \cos\phi' \boldsymbol{u}_y$ and $\boldsymbol{R} = (\rho - b_s\cos\phi')\boldsymbol{u}_x - b_s \sin\phi' \boldsymbol{u}_y + (z-z_s)\boldsymbol{u}_z$, as before, we have

$$d\boldsymbol{l}' \times \boldsymbol{R} = b_s(z-z_s)\cos\phi' d\phi' \boldsymbol{u}_x + b_s(z-z_s)\sin\phi' d\phi' \boldsymbol{u}_y + (b_s^2 - \rho b_s \cos\phi') d\phi' \boldsymbol{u}_z.$$

Substituting in (2.14) yields

$$\boldsymbol{B} = \frac{\mu_0 I}{4\pi} \int_0^{2\pi} \frac{[b_s(z-z_s)\cos\phi' \boldsymbol{u}_x + (b_s^2 - \rho b_s \cos\phi')\boldsymbol{u}_z] d\phi'}{[\rho^2 + b_s^2 - 2\rho b_s \cos\phi' + (z-z_s)^2]^{3/2}}. \tag{2.20}$$

$\boldsymbol{B}$ is calculated numerically by dividing the turn into a number of L elements as described in the previous section. Hence, the integration in (2.20) is converted into a summation, namely

$$\boldsymbol{B} = \frac{\mu_0 I}{4\pi} \sum_{i=1}^{L} \frac{[b_s(z - z_s)\cos\phi_i \boldsymbol{u}_x + (b_s^2 - \rho b_s \cos\phi_i)\boldsymbol{u}_z]\frac{2\pi}{L}}{[\rho^2 + b_s^2 - 2\rho b_s \cos\phi_i + (z - z_s)^2]^{3/2}} \tag{2.21}$$

where $\phi_i = \frac{2\pi}{L}(i-1)$. Again, like in the previous section, the magnetic flux density $\Delta\boldsymbol{B}$ at P produced by a narrow circular strip having a uniform surface current of density J_s and width Δw, located with its center line on the circular turn, is

$$\Delta\boldsymbol{B} = \frac{\mu_0 J_s \Delta w}{4\pi} \sum_{i=1}^{L} \frac{[b_s(z - z_s)\cos\phi_i \boldsymbol{u}_x + (b_s^2 - \rho b_s \cos\phi_i)\boldsymbol{u}_z]\frac{2\pi}{L}}{[\rho^2 + b_s^2 - 2\rho b_s \cos\phi_i + (z - z_s)^2]^{3/2}}. \tag{2.22}$$

2.2 Surface Impedance

The concepts of surface impedance and skin depth or depth of penetration are often used in the literature [4], associated with high frequency propagating electromagnetic waves though they are also used in quasistationary field problems. These concepts are introduced based on the behavior of time-harmonic electromagnetic fields in linear, homogeneous and isotropic media. Combining the Ohms law $\boldsymbol{J} = \sigma\boldsymbol{E}$, where σ is the conductivity in the medium, with (2.5) _ (2.1) and (2.6) _ (2.2), we obtain

$$\nabla \times \boldsymbol{H} = (\sigma + j\omega\epsilon)\boldsymbol{E} \tag{2.23}$$

and

$$\nabla \times \boldsymbol{E} = -j\omega\mu\boldsymbol{H}. \tag{2.24}$$

The substitution of (2.23) in (2.24) after taking curl both side of (2.24), gives

$$\nabla \times \nabla \times \boldsymbol{E} = k^2\boldsymbol{E} \tag{2.25}$$

where $k = \sqrt{-j\omega\mu(\sigma + j\omega\epsilon)}$ is called the wave number of the medium. k is usually written as

$$k = k' - jk''$$

where k', the real part of k, is the phase constant and k'', the imaginary part of k, is the attenuation constant. In a source free region equation (2.25) becomes

$$\nabla^2 \boldsymbol{E} + k^2 \boldsymbol{E} = 0. \tag{2.26}$$

Consider $\boldsymbol{E}$ to have only an x component independent of x and y. Then (2.26) reduces to

$$\frac{d^2 E_x}{dz^2} + k^2 E_x = 0. \tag{2.27}$$

This equation is the one-dimensional Helmholtz equation whose solutions are linear combinations of e^{jkz} and e^{-jkz}. Consider only e^{-jkz} which gives a forward travelling wave. Then,

$$E_x = E_0 e^{-jkz} = E_0 e^{-k''z} e^{-jk'z} \tag{2.28}$$

where E_0 is the amplitude of E_x at $z = 0$. The associated magnetic field intensity of E_x is obtained from (2.24) and has only a y component, namely

$$H_y = \frac{kE_0}{\omega\mu} e^{-jkz} = \frac{k}{\omega\mu} E_x. \tag{2.29}$$

For good conductors σ is much greater than $\omega\epsilon$ so that k is approximately equal to $\sqrt{-j\omega\mu\sigma}$. Then k' and k'' are equal to $\sqrt{\omega\mu\sigma/2}$. Thus , the attenuation of electromagnetic field penetrating into a good conductor is very high. For example, a 10 MHz wave would attenuate 97.89 percent in 0.1 mm of travel in aluminum. The field is practically constrained in a thin surface layer. This phenomenon is known as skin effect. The distance in which a wave is attenuated to 36.8 percent (1/e) of its initial value is called the skin depth or depth of penetration δ. Thus,

$$\delta = \frac{1}{k''} = \sqrt{\frac{2}{\omega\mu\sigma}} \tag{2.30}$$

For example, the depth of penetration in aluminum at 8 KHz is approximately 0.92 mm.

On a flat surface of a good conductor, the ratio of E_x to H_y is equivalent to the standard surface impedance, Z_s, when the wave is travelling normal to the conductor surface. According to (2.29), Z_s is equal to $\omega\mu/k$. This means that the tangential components of electric field and magnetic field on the conductor surface are related by

$$\boldsymbol{n} \times \boldsymbol{E} = -Z_s \boldsymbol{n} \times (\boldsymbol{n} \times \boldsymbol{H}) \tag{2.31}$$

where $\boldsymbol{n}$ is the inward normal unit vector to the surface. For an infinite conducting plane, The relation between Z_s and the δ is,

$$Z_s = \frac{1+j}{\sigma\delta}. \tag{2.32}$$

Even though (2.32) is strictly true for an infinite conducting plane, it can be used for conducing surfaces as well, provided that δk_v and δk_w are much less than one, where k_v and k_w are the principal curvatures. v and w are the principal curvature coordinates, with $\boldsymbol{u}_v \times \boldsymbol{u}_w = \boldsymbol{n}$ where $\boldsymbol{u}_v$ and $\boldsymbol{u}_w$ are unit vectors along the curves with constant v and w, respectively.

For finite radii of curvature, Leontovich has presented a first order curvature correction term in (2.30) and Mintzner [7] [10] has corrected it as

$$E_v = (1+p) Z_s H_w \tag{2.33}$$

$$E_w = -(1-p) Z_s H_v \tag{2.34}$$

where

$$p = 0.25(1+j)\delta(k_w - k_v). \tag{2.35}$$

Equations (2.33) and (2.34) are valid for any smooth surface.

2.3 Perfect Conductor Model

As discussed in the previous section, electromagnetic fields do not penetrate deep into conducting metals, especially at high frequencies, being confined to a very thin layer. In scattering problems, this phenomenon is approximated, in general, as fields interacting with perfect conductors because no electromagnetic field can exist inside perfect conductors. In the PC model Z_s is considered to be zero. In other words, tangential electric field on the surface is equal to zero. The tangential magnetic field intensity on the surface is equal in magnitude to the surface current density induced.

2.4 Method of Moments

Consider an inhomogeneous linear equation $L_o(f) = g$ where L_o is a linear operator, g is known and f is unknown. To determine f, it is expanded in a series of functions $f_1, f_2, f_3, ...$ as

$$f = \sum_{m=1}^{M} J_m f_m \tag{2.36}$$

where J_m are constant coefficients. f_m are called expansion functions or basis functions [5]. Considering the linearity of L_o, we can write $L_o(f) = g$ in the form $\sum_{m=1}^{M} J_m L_o(f_m) = g$. Then, the inner product of it with selected weighting functions w_n $(w_1, w_2, w_3, ..)$ in the range of L_o is taken on both sides, yielding

$$\sum_{m=1}^{M} J_m \langle w_n, L_o(f_m) \rangle = \langle w_n, g \rangle \tag{2.37}$$

From (2.37), a set of linear equations is obtained and written in matrix form as

$$[l_{nm}][J_m] = [g_n] \tag{2.38}$$

where

$$[l_{nm}] = \begin{bmatrix} \langle w_1, L_o(f_1)\rangle & \langle w_1, L_o(f_2)\rangle & \cdots & \langle w_1, L_o(f_M)\rangle \\ \langle w_2, L_o(f_1)\rangle & \langle w_2, L_o(f_2)\rangle & \cdots & \langle w_2, L_o(f_M)\rangle \\ \vdots & \vdots & \ddots & \vdots \\ \langle w_M, L_o(f_1)\rangle & \langle w_M, L_o(f_2)\rangle & \cdots & \langle w_M, L_o(f_M)\rangle \end{bmatrix}$$

$$[J_m] = \begin{bmatrix} J_1 \\ J_2 \\ \vdots \\ J_M \end{bmatrix}$$

and

$$[g_n] = \begin{bmatrix} \langle w_1, g\rangle \\ \langle w_2, g\rangle \\ \vdots \\ \langle w_M, g\rangle \end{bmatrix}.$$

There is a solution to $[J_m]$ if $[l_{nm}]$ is nonsingular. The evaluation of the inner product $\langle w_n, L_o(f_m)\rangle$ is often a tedious task in problems related to practical applications. Taking w_n to be the impulse function, approximate solutions can be obtained satisfying equation $L_o(f) = g$ at discrete point of interest. This procedure is known as point matching. For the simplicity, basis function f_m are selected such that they exist only over the subsections of the domain of f. The Garlerkin's procedure is implemented choosing $w_m = f_m$.

Chapter 3

Integral Equations for Arbitrarily Shaped Axisymmetric Conductors

Integral equations are formulated for arbitrarily shaped conductors with smooth surfaces in the presence of current-carrying coils. The formulation is general so that the PC, SI and MSI models can be implemented. The application of the method of moments to yield a set of linear equations is elaborated. Numerical evaluation of the integrals involved are described. Handling the singularities in their integrands is also given in this chapter. The calculation of power loss in the conductor and electromagnetic force upon it is explained in the last section.

3.1 Formulation

Consider an arbitrarily shaped axisymmetric good conductor having a smooth surface, as depicted in Fig. 3.1 in the presence of a quasistationary magnetic field produced by coaxial turns carrying sinusoidal with time currents of same frequency. As discussed earlier, at sufficiently small depths of penetration, the electromagnetic field can be analyzed by determining the equivalent surface current density which has an azimuthal $\phi-$direction.

Combining (2.13) and (2.9), the tangential electric field intensity produced by the inducing

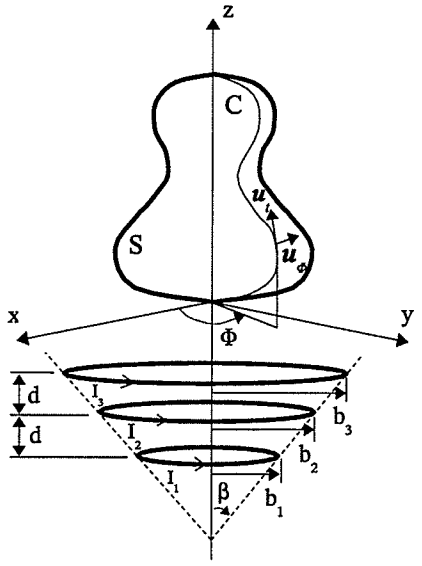

Figure 3.1: Solid conductor in the presence of current-carrying turns.

turns alone in free space is given by

$$\frac{-j\omega\mu_0}{4\pi}\sum_{k=1}^{N} I_k \boldsymbol{u}_\phi(\boldsymbol{r})\cdot\int_{C_k}\frac{d\boldsymbol{l}'}{R}$$

where $d\boldsymbol{l}'$ is the vector element in the direction of the current along the respective inducing turn C_k, carrying the current I_k and N is the total number of turns. The induced currents in the conductor which are again in the azimuthal $\phi-$ direction produce a tangential electric field equal to

$$\frac{-j\omega\mu_0}{4\pi}\boldsymbol{u}_\phi(\boldsymbol{r})\cdot\int_{S}\frac{\boldsymbol{J}_s(\boldsymbol{r}')ds'}{R}.$$

The total tangential electric field E_ϕ is a superposition of the field produced by the external turns and by the induced currents, *i.e*

$$E_\phi(\boldsymbol{r}) = \frac{-j\omega\mu_0}{4\pi}\left[\boldsymbol{u}_\phi(\boldsymbol{r})\cdot\int_{S}\frac{\boldsymbol{J}_s(\boldsymbol{r}')ds'}{R} + \sum_{k=1}^{K} I_k \boldsymbol{u}_\phi(\boldsymbol{r})\cdot\int_{C_k}\frac{d\boldsymbol{l}'}{R}\right]. \tag{3.1}$$

According to (2.14), the tangential magnetic field intensity due to the external turns is

$$\frac{1}{4\pi}\sum_{k=1}^{N} I_k \boldsymbol{u}_t(\boldsymbol{r}) \cdot \int_{C_k} \frac{d\boldsymbol{l}' \times \boldsymbol{R}}{R^3}$$

where $\boldsymbol{u}_t$ is the unit vector along the generator curve C of the conductor. The tangential magnetic field intensity due to the induced currents on the conductor surface is obtained from (2.15) as

$$\frac{1}{4\pi}\boldsymbol{u}_t(\boldsymbol{r}) \cdot \int_{S} \frac{\boldsymbol{J}_s(\boldsymbol{r}') \times \boldsymbol{R} ds'}{R^3}.$$

The total tangential magnetic field intensity produced by the external turns and by the induced currents is given by

$$H_t(\boldsymbol{r}) = \frac{1}{4\pi}\left[\boldsymbol{u}_t(\boldsymbol{r}) \cdot \int_{S} \frac{\boldsymbol{J}_s(\boldsymbol{r}') \times \boldsymbol{R} ds'}{R^3} + \sum_{k=1}^{N} I_k \boldsymbol{u}_t(\boldsymbol{r}) \cdot \int_{C_k} \frac{d\boldsymbol{l}' \times \boldsymbol{R}}{R^3}\right]. \tag{3.2}$$

The integral equation satisfied by $\boldsymbol{J}_s$ is constructed by imposing the condition that the tangential electric field intensity $E_\phi(\boldsymbol{r})$, at the conductor surface S, is related to the tangential magnetic field intensity $H_t(\boldsymbol{r})$ at the same point through the surface impedance $Z_s(\boldsymbol{r})$ as

$$E_\phi|_s = -Z_s(\boldsymbol{r}) H_t|_s. \tag{3.3}$$

The minus sign present in the above equation is due to the cross product $\boldsymbol{u}_\phi \times \boldsymbol{u}_t$ pointing outward from the surface. The surface integral equation formulated is rearranged keeping the unknown terms on one side of the equation and the known terms on the other side. The result is

$$-j\omega\mu_0\left[\boldsymbol{u}_\phi(\boldsymbol{r}) \cdot \int_{S} \frac{\boldsymbol{J}_s(\boldsymbol{r}') ds'}{R}\right] + Z_s(\boldsymbol{r})\boldsymbol{u}_t(\boldsymbol{r}) \cdot \int_{S} \frac{\boldsymbol{J}_s(\boldsymbol{r}') \times \boldsymbol{R} ds'}{R^3} =$$

$$\sum_{k=1}^{N} I_k \left[j\omega\mu_0 \boldsymbol{u}_\phi(\boldsymbol{r}) \cdot \int_{C_k} \frac{d\boldsymbol{l}'}{R} - Z_s(\boldsymbol{r})\boldsymbol{u}_t(\boldsymbol{r}) \cdot \int_{C_k} \frac{d\boldsymbol{l}' \times \boldsymbol{R}}{R^3}\right]. \tag{3.4}$$

The surface integral equation using the PC model is obtained from (3.4) by taking $Z_s(\boldsymbol{r}) = 0$. The simplest SI integral equation is obtained by using the standard surface impedance model, *ie.* $Z_s(\boldsymbol{r}) = Z_s$. The MSI integral equation is formed when $Z_s(\boldsymbol{r})$ is evaluated as in (2.33)-(2.35).

3.2 Solution Method

The above integral equation is solved by applying the point matching procedure. Due to the axisymmetric nature of the system, the induced current density has only a component in the ϕ-direction. The unknown current density is expressed in terms of M subdomain basis functions $f_m(t)$ as

$$\boldsymbol{J}_s = \boldsymbol{u}_\phi \sum_{m=1}^{M} J_m f_m(t) \tag{3.5}$$

where t is the length variable along C. $f_m(t)$ is considered to be a rectangular pulse function, as shown in the Fig. 3.2. In other words, the induced current density is approximated step-wisely, as depicted in Fig. 3.2. Then, each J_m in the expansion (3.5) affects the approximation of f only over a subsection of interest. The width of the pulse is Δw_m. The weighting function $w_n(t)$ in the point matching procedure is the Dirac delta function

$$w_n(t) = \delta(t - t_n) \tag{3.6}$$

which is a function only of the variable t due to the axisymmetry. For convenience, all the observation points on S are located on the x-z plane, $\phi = 0$. Substituting (3.5) into (3.4) and taking the inner product of (3.4) with $\delta(t - t_n)$ gives

$$-j\omega\mu_0 \left[\sum_{m=1}^{M} J_m \int_S \frac{f_m(t')ds'}{R_{mn}} \right] + Z_s(\boldsymbol{r}) \sum_{m=1}^{M} J_m \boldsymbol{u}_t(\boldsymbol{r}_n) \cdot \int_S \frac{f_m(t')\boldsymbol{u}_\phi(\boldsymbol{r}_m) \times \boldsymbol{R}_{mn} ds'}{R_{mn}^3} =$$

$$\sum_{k=1}^{N} I_k \left[j\omega\mu_0 \boldsymbol{u}_\phi(\boldsymbol{r}_n) \cdot \int_{C_k} \frac{d\boldsymbol{l}'}{R_{kn}} - Z_s(\boldsymbol{r}) \boldsymbol{u}_t(\boldsymbol{r}_n) \cdot \int_{C_k} \frac{d\boldsymbol{l}' \times \boldsymbol{R}_{kn}}{R_{kn}^3} \right] \tag{3.7}$$

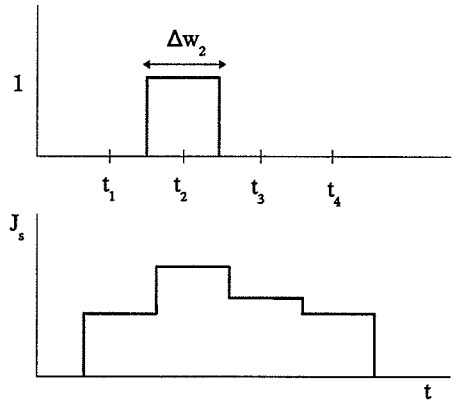

Figure 3.2: Pulse function and step approximation of current density.

where $\boldsymbol{R}_{mn}$ is the distance vector from the source point on S, related to f_m, to the observation point on S, related to t_n, $\boldsymbol{R}_{kn}$ is the distance vector from the source point on the inducing turn k to the observation point on S related to t_n, and $\boldsymbol{r}_n$ is the position vector of the observation point on S in the x-z plane at $t = t_n$. Equation (3.7) is a linear equation with a number M of unknowns. It is evident that a number M of linear equations are required to solve for these unknowns. M weighting functions at different observation points (t_n, $n = 1$ to M) are used to obtain the required number of linear equations in the form $[l_{mn}][J_m] = [g_n]$. All observation points are chosen to be the midpoints of the corresponding rectangular pulse functions.

3.2.1 Discretization

A physical interpretation of (3.7) gives an additional insight into the method of moments. Consider the first term in the left hand side of (3.7). For a particular m, it is proportional to the tangential electric field at the observation point on the surface, having a position vector $\boldsymbol{r}_n$ and being produced by a circular strip of width Δw_m, carrying a uniform current

density J_m. The second term in the left hand side of the equation is proportional to the magnetic field intensity tangential to the generator curve C at the same observation point, produced by a circular strip carrying the uniform current density J_m. This means that the current distribution on the conductor surface is approximated by M coaxial circular strips, each carrying a uniformly distributed current. These two integrals are solved numerically.

The contribution to the tangential electric and magnetic field intensities at a point on the surface is evaluated by assuming that the current of each strip is concentrated on its center line, except where the source point coincides with the observation point. The surface integrals in (3.7) are taken in principal values when the source point coincides with the observation point. The next section describes how singularities are evaluated. Each strip is divided into a number of elements in order to evaluate their electric and magnetic field intensities. Equations (2.19) and (2.22) are used to calculate the electric field intensity and the magnetic field intensity on the surface, where the source point does not coincide with the observation point.

The generator curve C of the conductor may not be represented by a well defined function. So the surface of the conductor is defined by specifying the radius x_m of the circle at the center plane $z = z_m$ of each circular strip, the width of the strip, Δw_m, and the angle α_m between the z-axis and the normal vector to the surface at (x_m,0,z_m). α_m is measured from the z axis. $\boldsymbol{u}_n(x_m, 0, z_m)$ and $\boldsymbol{u}_t(x_m, 0, z_m)$ are the unit normal vector and the unit tangential vector in the x-z plane, respectively. Then, we have

$$\boldsymbol{u}_x \cdot \boldsymbol{u}_t(x_m, 0, z_m) = -\cos\alpha_m \qquad \boldsymbol{u}_z \cdot \boldsymbol{u}_t(x_m, 0, z_m) = \sin\alpha_m \tag{3.8}$$

$$\boldsymbol{u}_x \cdot \boldsymbol{u}_n(x_m, 0, z_m) = \sin\alpha_m \qquad \boldsymbol{u}_z \cdot \boldsymbol{u}_n(x_m, 0, z_m) = \cos\alpha_m \tag{3.9}$$

It is obvious that $\boldsymbol{u}_y \cdot \boldsymbol{u}_t(x_m, 0, z_m) = 0$. Substituting (2.19), (2.22) and (3.8) into (3.7), the

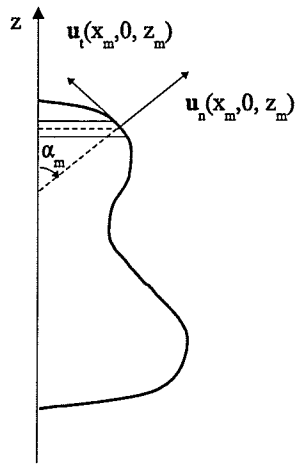

Figure 3.3: Normal and tangential unit vectors to the surface.

matrix element l_{nm} is obtained as given in (3.10).

$$\begin{aligned} l_{nm}|_{n\neq m} =& \frac{-j2\pi\omega\mu_0\Delta w_m}{L}\sum_{i=1}^{L}\frac{x_m\cos\phi_i}{\sqrt{x_n^2+x_m^2-2x_nx_m\cos\phi_i+(z_n-z_m)^2}} \\ &+\frac{2\pi Z_s(\boldsymbol{r}_n)\Delta w_m}{L}\sum_{i=1}^{L}\frac{\left[-x_m(z_n-z_m)\cos\alpha_n\cos\phi_i+\sin\alpha_n(x_m^2-x_mx_n\cos\phi_i)\right]}{\left[x_n^2+x_m^2-2x_nx_m\cos\phi_i+(z_n-z_m)^2\right]^{3/2}} \end{aligned} \tag{3.10}$$

where $\phi_i = 2\pi/L$. $Z_s(\boldsymbol{r}_n)$ is independent of $\boldsymbol{r}_n$ unless the surface impedance is modified as discussed in section 2.2.

The first and the second terms on the right side of (3.7) are proportional to the electric and magnetic field intensities at the same observation point on S, produced by the external current carrying turns. The elements of the column matrix $[g_n]$ are also written as a summation by substituting (2.18), (2.21) and (3.8) into (3.7). The result is

$$\begin{aligned} g_n =& \frac{2\pi}{L}\sum_{k=1}^{N}I_k\Bigg[-Z_s(\boldsymbol{r}_n)\sum_{i=1}^{L}\frac{-b_k(z_n-z_k)\cos\alpha_n\cos\phi_i+\sin\alpha_n(b_k^2-b_kx_n\cos\phi_i)}{\left[x_n^2+b_k^2-2x_nb_k\cos\phi_i+(z_n-z_k)^2\right]^{3/2}} \\ &+j\omega\mu_0\sum_{i=1}^{L}\frac{b_k\cos\phi_i}{\sqrt{x_n^2+b_k^2-2x_nb_k\cos\phi_i+(z_n-z_k)^2}}\Bigg], \end{aligned} \tag{3.11}$$

where b_k is the radius of k-th inducing turn.

3.2.2 Singularities

The calculation of l_{nn} requires special treatment in order to evaluate singularities. These singularities appear in (3.10) when $i = 1$ and $m = n$. The contribution of each rectangular self-patch of dimension g'-by-h' to the electric field intensity E'_ϕ at its center is given by

$$E'_\phi = -\frac{j\omega\mu_0 J_s}{2\pi}\left[g' \ln\left(\frac{h'}{g'} + \sqrt{1+\frac{h'^2}{g'^2}}\right) + h' \ln\left(\frac{g'}{h'} + \sqrt{1+\frac{g'^2}{h'^2}}\right)\right]. \tag{3.12}$$

The derivation of (3.12) is listed in Appendix A.

The contribution of the same self-patch to the magnetic field intensity H'_t at its center is given by [5]

$$H'_t = -\frac{J_s}{2}. \tag{3.13}$$

Then the diagonal elements of the matrix $[l_{nm}]$ are evaluated as

$$\begin{aligned} l_{nn} =& 4\pi E'_\phi + 4\pi Z_s(\boldsymbol{r}_n) H'_t - \frac{j2\pi\omega\mu_0\Delta w_n}{L}\sum_{i=2}^{L}\frac{\cos\phi_i}{\sqrt{2(1-\cos\phi_i)}} \\ &+ \frac{\pi Z_s(\boldsymbol{r}_n)\Delta w_n}{L}\sum_{i=2}^{L}\frac{\sin\alpha_n}{x_n\sqrt{2(1-\cos\phi_i)}}. \end{aligned} \tag{3.14}$$

Once all the elements of the matrixes $[l_{nm}]$ and $[g_n]$ are evaluated, the unknown current density matrix $[J_n]$ can be found from (3.7).

3.3 Calculation of Power Loss and Force

Losses in conducting objects at high frequencies can be evaluated using the surface resistance R_s for both the PC and SI models, considering the actual conductivity σ of the material. The time-average power loss is

$$P = \frac{1}{2}\int_S R_s |J_s|^2 ds. \tag{3.15}$$

This integral is converted into a summation to evaluate it numerically, as

$$P = \pi R_s \sum_{m=1}^{M} \Delta w_m |J_m|^2 x_m \tag{3.16}$$

The electromagnetic force acting upon the conducting body is evaluated by calculating the resulting total force upon the inducing turns, which is the same in magnitude but opposite in direction. The resultant time-average force exerted upon the system of inducing turns is expressed as

$$\boldsymbol{F} = \frac{1}{2} Re\left[\sum_{k=1}^{N} I_k \int_{C_k} (\boldsymbol{u}_\phi \times \boldsymbol{B}_k^*) dl\right] = -\boldsymbol{u}_z \pi \sum_{k=1}^{N} b_k Re(I_k B_k^*) \tag{3.17}$$

where the asterisk indicates the complex conjugate and $\boldsymbol{B}_k$ is the outwardly oriented radial component of the magnetic flux density produced only by the induced currents in the conducting body at the points on the k-th inducing turn.

Chapter 4

Integral Equations for Spherical Conductors

In this chapter, integral equations are formulated for spherical conductors in the presence of current-carrying turns. The evaluation of the tangential electric and magnetic field components on the conductor surface can be performed by employing the spherical coordinate system. The electric field intensity and the magnetic flux density produced by a current-carrying turn are determined in the first section. In section 3, numerical results for power loss and electromagnetic force upon the conductor obtained from the SI and PC integral equations are compared with their exact analytical results [17]. The accuracy of the results are improved by employing a finer mesh. The last section compares the performance of Garlerkin's method against the point matching.

4.1 Electric Field Intensity and Magnetic Flux Density in Spherical Coordinates Produced by a Current-Carrying Turn

The electric field intensity and the magnetic flux density produced by a single turn carrying sinusoidal current I are found in spherical coordinates for the turn placed as shown in Fig.

4.1. The magnitude of the position vector of a point on the turn is r_s. The angle between the z-axis and the position vector of the point on the turn is θ_s. The coordinates of the observation point in the x-z plane are $(r_p,\theta_p,0)$. The vector length element on the turn at the source point, $(r_s,\ \theta_s,\ \phi')$, is $d\boldsymbol{l}'$ where $d\boldsymbol{l}' = -r_s \sin\theta_s \sin\phi' d\phi' \boldsymbol{u}_x + r_s \sin\theta_s \cos\phi' d\phi' \boldsymbol{u}_y$. The distance between the source point and the observation point is given by

$$R = \sqrt{r_p^2 + r_s^2 - 2r_p r_s(\sin\theta_p \sin\theta_s \cos\phi' + \cos\theta_p \cos\theta_s)}.$$

The vector potential is calculated substituting $d\boldsymbol{l}'$ and R into (2.13). Using (2.9), the electric field intensity is found as

$$E_\phi = -\frac{j\omega\mu_0 I}{4\pi} \int_0^{2\pi} \frac{r_s \sin\theta_s \cos\phi' d\phi'}{R}. \tag{4.1}$$

This integral is evaluated numerically discretizing the turn into a number of L elements as

$$E_\phi = -\frac{j\omega\mu_0 I}{4\pi} \sum_{i=1}^{L} \frac{r_s \sin\theta_s \cos\phi_i (2\pi/L)}{R_i} \tag{4.2}$$

where $R_i = \sqrt{r_p^2 + r_s^2 - 2r_p r_s(\sin\theta_p \sin\theta_s \cos\phi_i' + \cos\theta_p \cos\theta_s)}$ and $\phi_i = (2\pi/L)(i-1)$.

Equation (4.2) is modified as discussed in section 2.1.2 to obtain the electric field intensity produced by a circular current-carrying strip,

$$E_\phi = -\frac{j\omega\mu_0 r_s \Delta\theta_s J_s}{4\pi} \sum_{i=1}^{L} \frac{r_s \sin\theta_s \cos\phi_i (2\pi/L)}{R_i} \tag{4.3}$$

where $r_s\Delta\theta_s$ is the width of the strip.

The magnetic flux density produced by a current carrying turn is obtained using (2.14). The distance vector $\boldsymbol{R}$ from the source point to the observation point is given by

$$\boldsymbol{R} = (r_p \sin\theta_p - r_s \sin\theta_s \cos\phi')\boldsymbol{u}_x - r_s \sin\theta_s \sin\phi' \boldsymbol{u}_y + (r_p \cos\theta_p - r_s \cos\theta_s)\boldsymbol{u}_z.$$

Substituting $d\boldsymbol{l}' \times \boldsymbol{R}$ and R into (2.14), we obtain

$$\begin{aligned} \boldsymbol{B} = \frac{\mu_0 I}{4\pi} \int_0^{2\pi} \frac{1}{R^3} \Big[& r_s \sin\theta_s (r_p \cos\theta_p - r_s \cos\theta_s) \cos\phi' \boldsymbol{u}_x \\ & + (r_s^2 \sin^2\theta_s - r_p r_s \sin\theta_p \sin\theta_s \cos\phi')\boldsymbol{u}_z \Big] d\phi' \end{aligned} \tag{4.4}$$

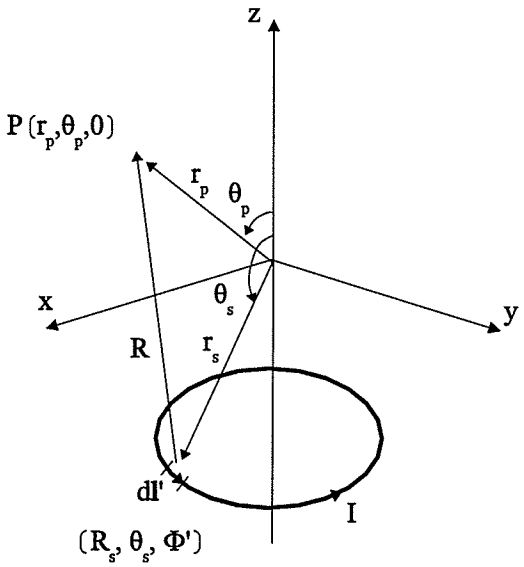

Figure 4.1: Source points and the observation point in spherical coordinates.

which is evaluated numerically by discretizing the turn into L elements as described in Section 2.1. Using (A.2), (A.3) and (A.4), the θ-directed flux density B_θ is obtained by taking the dot product $\boldsymbol{u}_\theta \cdot \boldsymbol{B}$, namely

$$B_\theta = \frac{\mu_0 I}{4\pi} \sum_{i=1}^{L} \frac{1}{R_i^3} \Big[r_s \sin\theta_s (r_p \cos\theta_p - r_s \cos\theta_s) \cos\theta_p \cos\phi_i - r_s \sin\theta_s \sin\theta_p (r_s \sin\theta_s - r_p \sin\theta_p \cos\phi_i) \Big] \frac{2\pi}{L} \tag{4.5}$$

where $\boldsymbol{u}_\theta$ is the unit vector in the θ-direction.B_θ produced by the circular strip considered above is computed from

$$B_\theta = \frac{\mu_0 r_s \Delta\theta_s J_s}{4\pi} \sum_{i=1}^{L} \frac{1}{R_i^3} \Big[r_s \sin\theta_s (r_p \cos\theta_p - r_s \cos\theta_s) \cos\theta_p \cos\phi_i - r_s \sin\theta_s \sin\theta_p (r_s \sin\theta_s - r_p \sin\theta_p \cos\phi_i) \Big] \frac{2\pi}{L}. \tag{4.6}$$

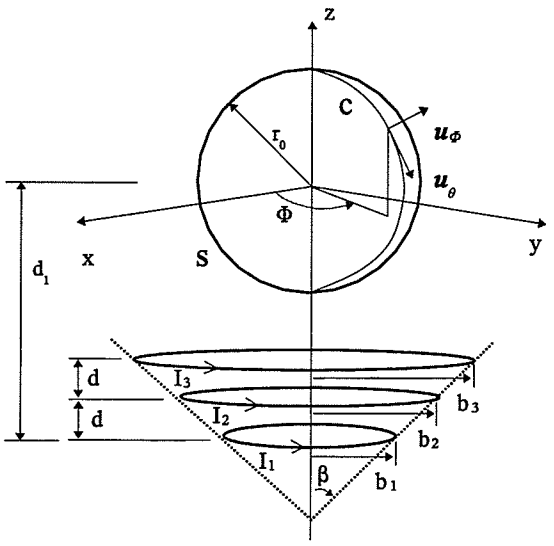

Figure 4.2: Spherical conductor in the presence of current-carrying turns.

4.2 Formulation

The integral equations are formulated for a spherical conductor in the magnetic field produced by coaxial turns carrying sinusoidal with time currents of the same frequency, as shown in Fig. (4.2). Using (2.9), (2.12) and (2.13), the total tangential electric field intensity at a point on S is given by

$$E_\phi = -\frac{j\omega\mu_0}{4\pi}\left[\int_0^\pi\int_0^{2\pi}\frac{J_s(\theta')r_0^2\sin\theta' d\phi' d\theta'}{R_1} + \sum_{k=1}^{N} I_k \int_0^{2\pi}\frac{r_k \sin\theta_k \cos\phi' d\phi'}{R_k}\right] \tag{4.7}$$

where R_1 is the distance between a source point and the observation point on the sphere surface, and R_k is the distance between a source point on turn k and the observation point on the conductor. The tangential magnetic field intensity at the same observation point is given in (4.8).

$$H_\theta = \frac{1}{4\pi}\left[\boldsymbol{u}_\theta \cdot \int_0^\pi\int_0^{2\pi}\frac{J_s(\boldsymbol{u}_\phi(\phi')\times\boldsymbol{R}_1)r_0^2\sin\theta' d\phi' d\theta'}{R_1^3} + \sum_{k=1}^{N} I_k \boldsymbol{u}_\theta \cdot \int_0^{2\pi}\frac{(\boldsymbol{u}_\phi(\phi')\times\boldsymbol{R}_k)r_k\sin\theta_k d\phi'}{R_k^3}\right] \tag{4.8}$$

The tangential electric field intensity E_ϕ and the tangential magnetic field intensity H_θ are related through the standard surface impedance as,

$$\frac{E_\phi}{H_\theta} = Z_s. \tag{4.9}$$

4.3 Application of Point Matching Procedure

A set of linear equations $[l_n][J_m] = [g_n]$ is obtained by applying the point matching procedure to solve the integral equation. The surface current density is approximated by rectangular single pulses. Dirac delta function is selected as the weighting function. Hence, the integral equation is transformed into a system of algebraic equations by discretizing the conductor surface into a number of M circular current-carrying strips. Each such circular strip and each inducing turn is divided into a number of elements to evaluate their electric and magnetic field intensities. The contributions to field intensities from circular strips are calculated by assuming that the current density is concentrated at the center of each element except when a singularity is present. Using (4.3), (4.6) and (4.9), the matrix element l_{nm} is obtained as

$$\begin{aligned} l_{nm}|_{n\neq m} = &- \frac{2\pi j\omega\mu_0 r_0^2 \Delta\theta_m}{L} \sum_{i=1}^{L} \frac{\sin\theta_m \cos\phi_i}{R_{mi}} \\ &- \frac{2\pi Z_s r_0^3 \sin\theta_m \Delta\theta_m}{L} \sum_{i=1}^{L} \frac{1}{R_{mi}^3} \Big[(\cos\theta_n - \cos\theta_m)\cos\theta_n \cos\phi_i \\ &- (\sin\theta_m - \sin\theta_n \cos\phi_i)\sin\theta_n \Big] \end{aligned} \tag{4.10}$$

where R_{mi} is the distance from the center point of the i-th element on the m-th strip to the observation point on the n-th strip. The width of the strip is $r_0\Delta\theta_m$. The element g_n of the column matrix $[g_n]$ is found to be

$$\begin{aligned} g_n = &\frac{2\pi j\omega\mu_0}{L} \sum_{k=1}^{N} I_k \sum_{i=1}^{L} \frac{r_k \sin\theta_k \cos\phi_i}{R_{ki}} + \frac{2\pi Zs}{L} \sum_{k=1}^{N} I_k \sum_{i=1}^{L} \frac{1}{R_{ki}^3} \Big[r_k \sin\theta_k (r_0 \cos\theta_n \\ &- r_k \cos\theta_k)\cos\theta_n \cos\phi_i - r_k (r_k \sin\theta_k - r_0 \sin\theta_n \cos\phi_i)\sin\theta_k \sin\theta_n \Big] \end{aligned} \tag{4.11}$$

where R_{ki} is the distance from the center point of the i-th element on the k-th inducing turn to the observation point on the n-th strip. The diagonal element l_{nn} is evaluated by treating the singularities as described in chapter 3. The unknown current density is found from $[l_{nm}]^{-1}[g_n]$. The solutions of the PC integral equation is determined taking $Z_s = 0$.

Numerical results are generated for aluminum ($\sigma = 3.77 \times 10^7$ S/m) spheres in the presence of three coaxial turns connected in series and carrying a current I_0. The three turns are placed on the surface of a cone of opening 2β, as shown in figure 4.2, the distance between the plane of the lower turn and the sphere center being d_1. To illustrate the performance of the surface integral equation in (4.9), the power loss and the electromagnetic force upon various spheres are evaluated using (3.16) and (3.17), respectively.

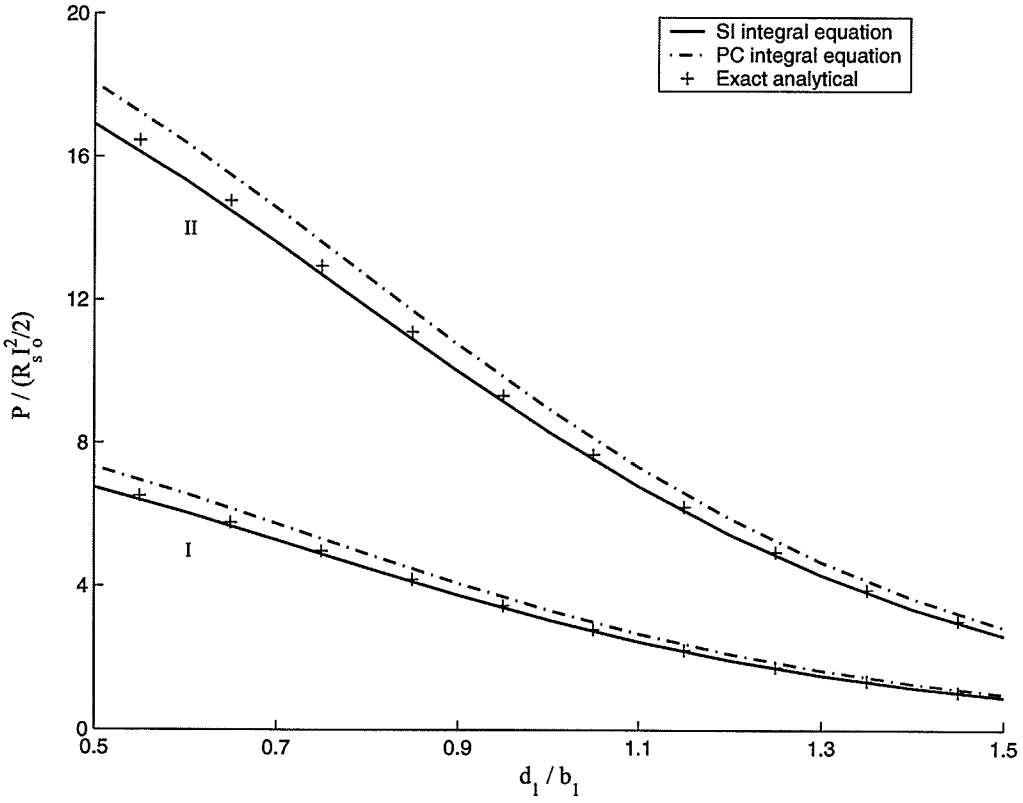

Figure 4.3: Normalized power loss versus d_1/b_1 for an aluminum sphere of radius $r_0 = 2.5$cm at 8 kHz, with $N = 3$, $\tan\beta = 0.4$, and $d/b_1 = 0.25$: (I) $r_0/b_1 = 0.5$; (II) $r_0/b_1 = 0.75$.

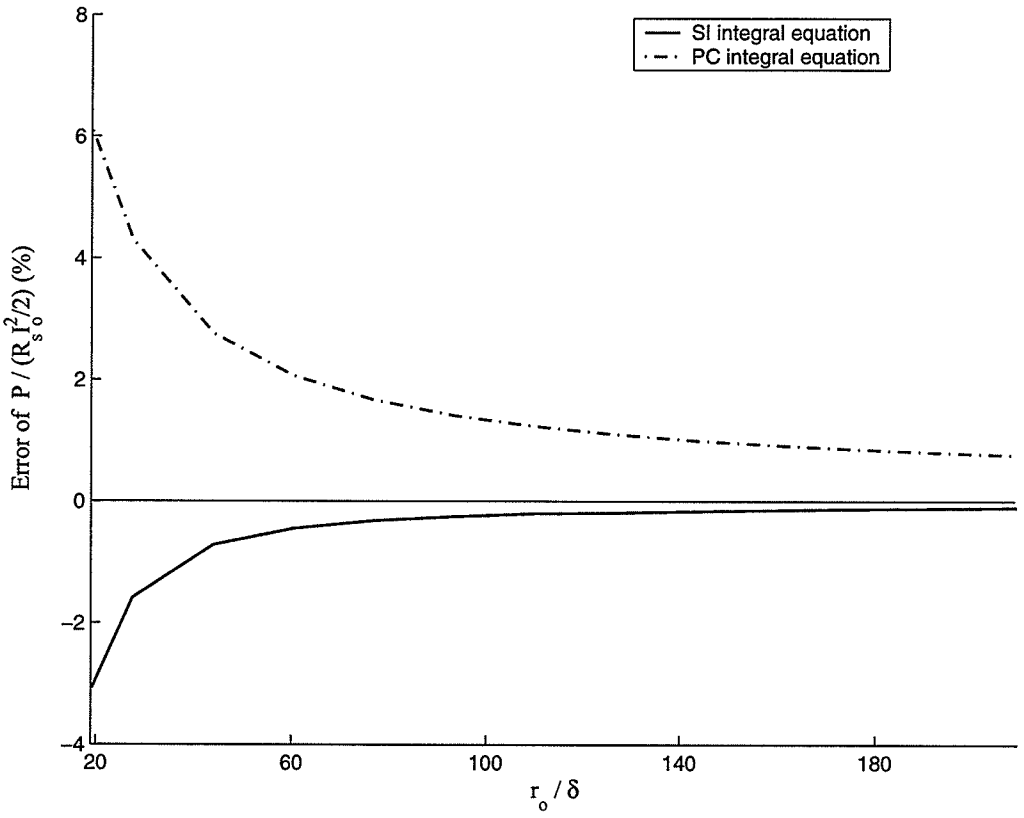

Figure 4.4: Error of the normalized power loss versus r_0/δ for aluminum spheres at 8 kHz, with $N = 3$, $\tan\beta = 0.4$, $d/b_1 = 0.25$, $d_1/b_1 = 0.6$ and $r_0/b_1 = 0.5$.

The time-average power loss normalized to $R_s I_0^2/2$, at a frequency of 8 kHz, with $N = 3$, $\tan\beta = 0.4$, $d/b_1 = 0.25$ for a sphere of radius $r_0 = 2.5$ cm is given in Fig. 4.3 as a function of the normalized distance between the sphere center and the inducing turns. The percentage error of the normalized power loss calculated from the integral equations with respect to the exact analytical solution for aluminum spheres is plotted in Fig. 4.4 versus the ratio of the sphere radius to the depth of penetration δ. The error decreases when the size of sphere increases. An accuracy of at least 97 percent has been achieved for the power loss by using the SI integral equation for spheres with r_0/δ above 20, while the errors introduced when using the PC integral equation are higher. The surfaces of the spheres have been discretized

into coaxial circular strips whose width is about 10 times the depth of penetration and each strip has been divided into a number of elements such that the element length was about 10 times the depth of penetration, with at least 10 elements per strip.

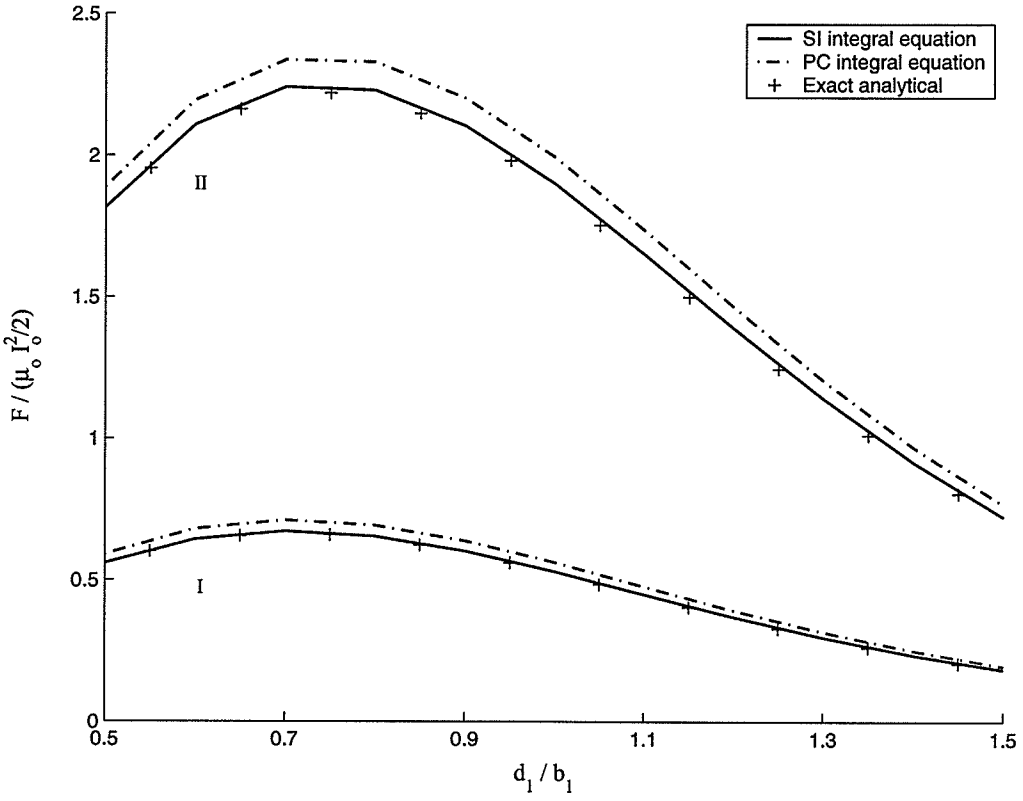

Figure 4.5: Normalized force versus d_1/b_1 for an aluminum sphere of radius $r_0 = 2.5$cm at 8 kHz, with $N = 3$, $\tan\beta = 0.4$, and $d/b_1 = 0.25$: (I) $r_0/b_1 = 0.5$; (II) $r_0/b_1 = 0.75$.

In Fig. 4.5, we compare the time-average electromagnetic force normalized to $\mu_0 I_0^2/2$ obtained by using the SI and the PC models with that from the exact analytical solution for the sphere system considered in Fig. 4.3. The percentage error of the normalized force obtained from the integral equations with respect to the exact analytical solutions for various sizes of spheres is shown in Fig. 4.6. The conductor surface entails 30 strips and each strip entails 60 elements. An accuracy of over 99 percent has been achieved by using the SI integral

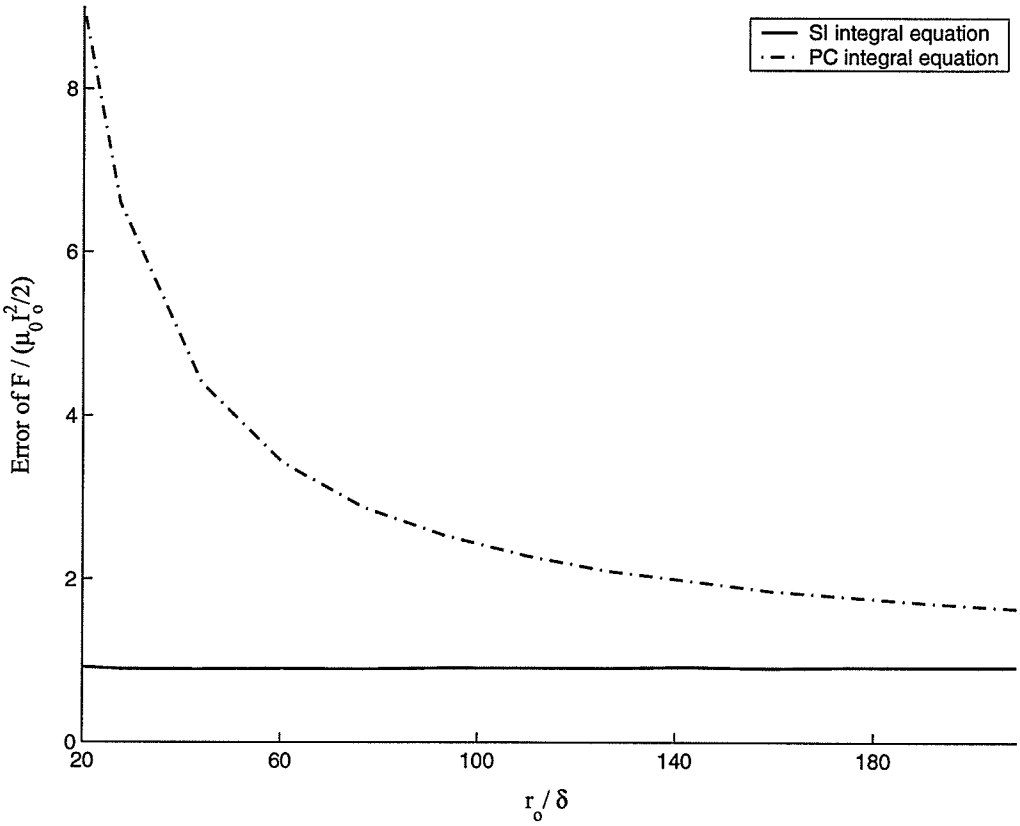

Figure 4.6: Error of the normalized force versus r_0/δ for aluminum spheres at 8 kHz, with $N = 3$, $\tan\beta = 0.4$, $d/b_1 = 0.25$, $d_1/b_1 = 0.6$ and $r_0/b_1 = 0.5$.

equation for calculating the force upon spheres with r_0/δ above 20. The error associated with the PC integral equations for evaluating the force upon spheres with r_0/δ below 20 is very high.

The normalized power losses in a sphere with $r_0 = 14$ cm at frequencies of 0.5 kHz and 2 kHz, with $N = 3$, $\tan\beta = 0.4$, $d/b_1 = 0.25$ and $b_0/b_1 = 0.5$ are depicted in Fig. 4.7. The normalized power loss evaluated from the PC integral integral equation is independent of the frequency, while the power loss evaluated from the SI integral equation and exact analytical method increases with frequency. Fig. 4.8 illustrates the variation of the normalized force with the ratio d_1/b_1 at frequencies of 0.5 kHz and 2 kHz for the same system as in Fig. 4.7.

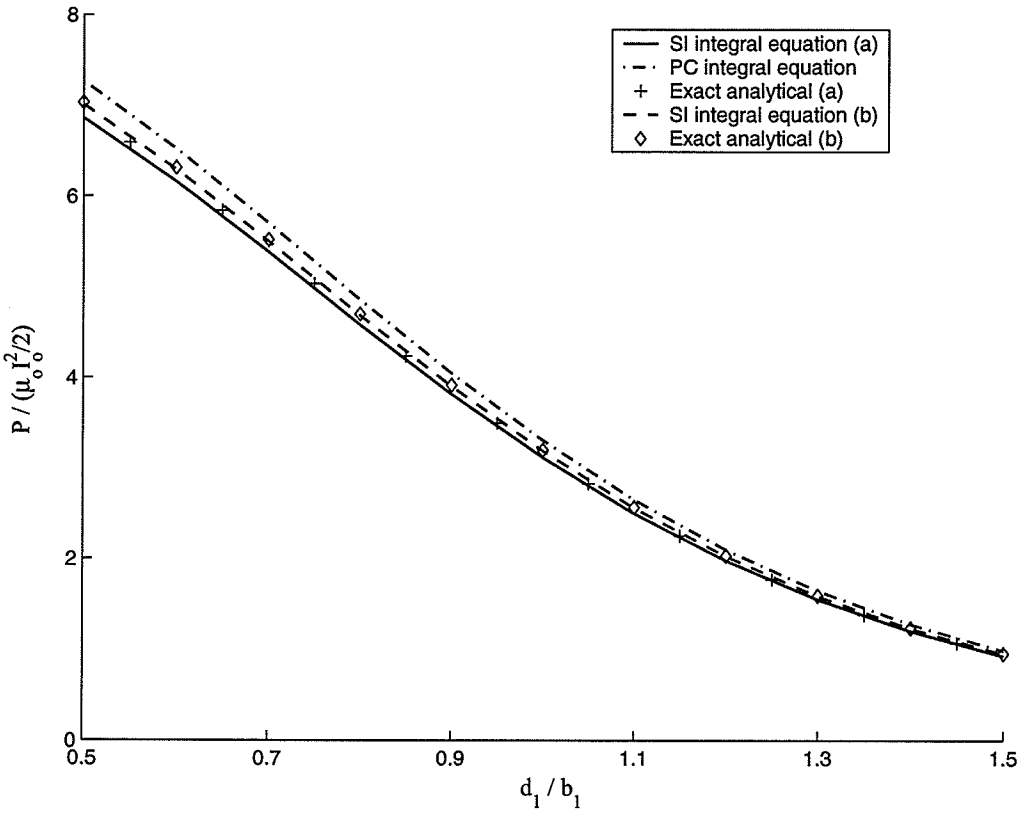

Figure 4.7: Normalized power loss versus d_1/b_1 for an aluminum sphere of radius $r_0 = 14$cm, with $N = 3$, $\tan\beta = 0.4$, $d/b_1 = 0.25$ and $r_0/b_1 = 0.5$ at (a) 0.5 kHz; (b) 2 kHz.

The normalized force obtained from the SI integral equations and from the exact analytical method increases with the frequency. The normalized force calculated from the PC integral equation is independent of frequency. The results based on the SI model are much closer to the exact analytical solution than the results based on the PC model.

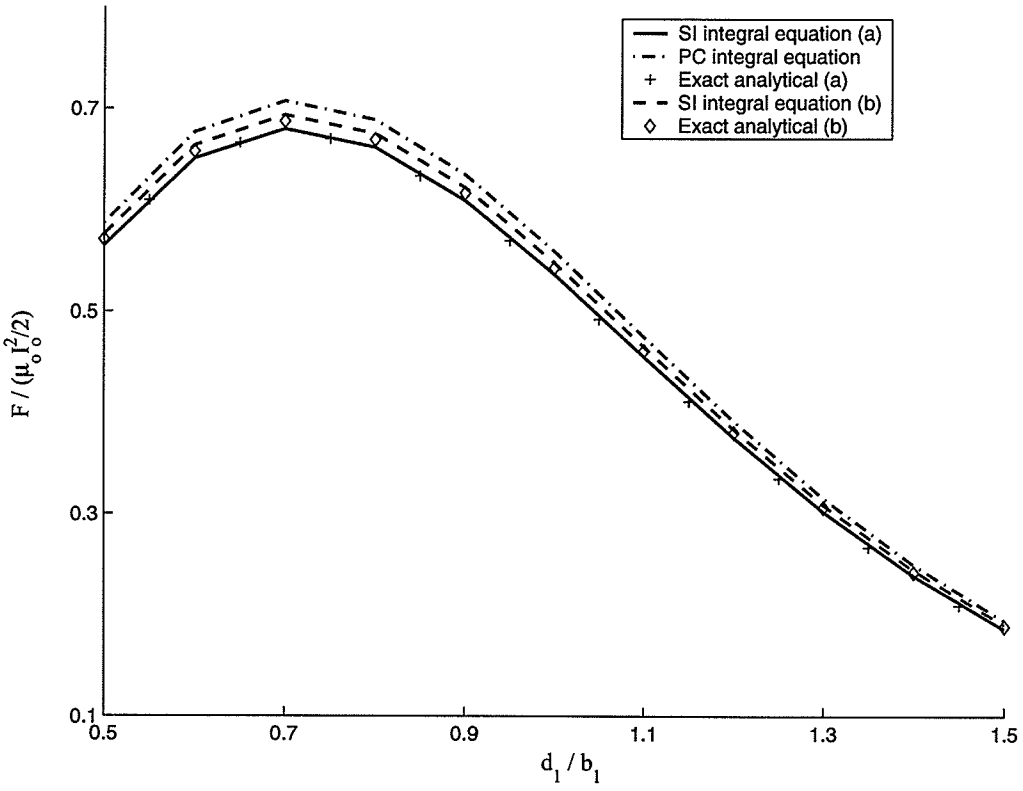

Figure 4.8: Normalized force versus d_1/b_1 for an aluminum sphere of radius $r_0 = 14$ cm, with $N = 3$, $\tan\beta = 0.4$, $d/b_1 = 0.25$ and $r_0/b_1 = 0.5$ at (a) 0.5 kHz; (b) 2 kHz.

4.3.1 Refining the Mesh for Spheres

When calculating the electric and the magnetic field intensities from neighboring patches, errors are introduced due to the fact that current density is considered to be concentrated on the center of the patch. A finer mesh is constructed by dividing the circular strips into 10 sub-strips in order to improve the accuracy. Each sub-strip of the circular strip carries the same current density J_m. The contribution to the electric and the magnetic field intensities at the observation point is found by summing up individual contributions from the 10 sub-strips. When evaluating individual contributions to the field intensities by a sub-strip, the current density is considered to be concentrated at the center line of that sub-strip.

A sphere of radius $r_0 = 14$ cm at a frequency of 8 kHz, with $N = 3$, $\tan\beta = 0.4$ and $d/b_1 = 0.25$, is considered to determine the effectiveness of the finer mesh. The normalized force has been evaluated using the SI integral equation for four cases and given in the Table 4.1. The percentage deviation of the force with respect to the SI analytical results and the computation time are compared for different cases. Computational time refers to a personal computer with Pentium IV processor. It is evident that subdividing only 10 neighboring strips makes significant improvement of the results. To obtain the same accuracy without subdividing the strips, the number M of strips and the number L of patches of each strip have to be increased to twice of that in the case of subdividing only 10 neighboring strips. Furthermore, the evaluation with increased M and L takes more computing time. The percentage error of the results obtained subdividing all strips has decreased only by 0.04 percent, while consuming more CPU time as compared with that when subdividing only the neighboring strips.

Table 4.1: Percentage deviation of force with respect to SI analytical solution.

Case	Percentage deviation	Computing time (s)
$M = 30$ $L = 60$ without subdividing strips	0.9	0.3
$M = 60$ $L = 120$ without subdividing strips	0.45	1.41
$M = 30$ $L = 60$ subdividing 10 neighboring strips	0.45	0.68
$M = 30$ $L = 60$ subdividing all strips	0.41	1.44

4.3.2 First Order Surface Impedance Correction for Spherical Conductors

The equations to modify the surface impedance for smooth boundaries given by Mitzner are presented in chapter 2. We choose $\boldsymbol{u}_v = \boldsymbol{u}_\phi$ and $\boldsymbol{u}_w = \boldsymbol{u}_\theta$ directing $\boldsymbol{u}_v \times \boldsymbol{u}_w$ inward to the surface. Equation (2.33) is selected in order to obtain the relation between E_ϕ and H_θ with modified surface impedance. Radii of curvature k_w and k_v are equal to $1/r_0$ [16].Hence, p in (2.33) becomes null. This implies that the first order correction of the surface impedance is already taken into account for spherical conductors.

4.4 Applying Galerkin's Method for Spheres

Numerical results for power losses and forces for spheres are also evaluated choosing $f_m(t)$ and $w_n(t)$ to be functions consisting of three constrained pulses [5] as shown in Fig. 4.9. The

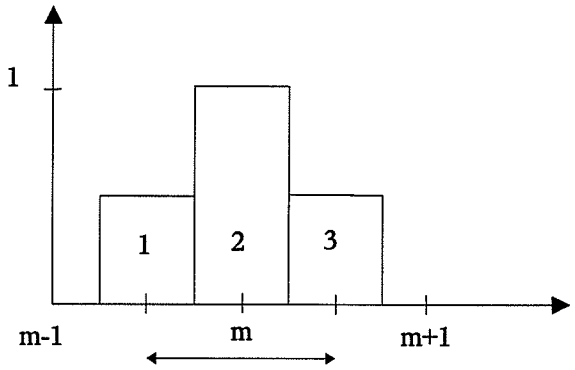

Figure 4.9: Expansion function consisting of three constrained pulses.

three pulses of each $f_m(\theta)$ and $w_n(\theta)$ are taken with the peak values of the side pulses equal to half of the peak value of the middle pulse. Then, the matrix element l_{nm} is expressed as

$$l_{nm} = \frac{1}{2}A_{n_2m_2} + \frac{1}{4}\Big(A_{n_2m_1} + A_{n_1m_2} + A_{n_2m_3} + A_{n_3m_2}\Big) + \frac{1}{4}\Big(A_{n_1m_1} + A_{n_1m_3} + A_{n_3m_1} + A_{n_3m_3}\Big) \tag{4.12}$$

where $A_{n_im_k} = E_{n_im_k} - Z_sH_{n_im_k}$, $E_{n_im_k}$ and $H_{n_im_k}$ being the electric and magnetic field intensities on the sphere surface at the center of the i-th pulse of $w_n(\theta)$ due to the k-th pulse of $J_mf_m(\theta)$; $i,k = 1,2,3$. $E_{n_im_k}$ and $H_{n_im_k}$ are calculated as in the previous case where rectangular basis functions and impulse functions are used.The column matrix element g_n is expressed in the form

$$g_n = \sum_{s=1}^{N} \frac{1}{2}A_{sn_2} + \frac{1}{4}\Big(A_{sn_1} + A_{sn_3}\Big) \tag{4.13}$$

where $A_{sn_k} = Z_sH_{sn_k} - E_{sn_k}$, E_{sn_k} and H_{sn_k} being the electric and magnetic field intensities on the center of the k-th pulse of $w_n(\theta)$ due to the s-th inducing turn. Table 4.2 compares the

number of basis functions required to obtained the same accuracy implementing Galerkin's method and the point matching procedure for a sphere of radius $r_0 = 25$ cm at the frequency 8 kHz, with $N = 3$, $\tan\beta = 0.4$, $d/b_1 = 0.25$, $d_1/b_1 = 0.6$ and $r_0/b_1 = 0.5$. The number of basis functions consisting of one rectangular pulse required to achieved the same accuracy has to be increased to about twice the number of basis functions consisting of three constrained rectangular pulses.

Table 4.2: Comparison of basis functions required for the same accuracy of Galerkin's solution and the point matching solution for SI integral equations.

Number of basis functions in Galerkin's method	Number of basis functions in point matching method
10	20
15	31
20	39

Chapter 5

Integral Equations for Prolate Spheroids

Integral equations are formulated for prolate spheroidal conductors in the presence of current-carrying turns. These inducing turns are placed axisymmetrically. The system of orthogonal curvilinear coordinates of the prolate spheroid is employed for analyzing the system considered.

The first section describes the prolate spheroidal coordinate system. The evaluation of electric and magnetic fields in prolate coordinates produced by inducing turns is described in section 5.2. The SI and PC integral equations are solved using both the point matching and Galerkin's methods. Numerical results are compared with available experimental data. The accuracy is improved using a finer mesh. In the last section, results from the SI and the MSI integral equations are compared with experimental data.

5.1 Introduction to Prolate Spheroidal Coordinates

The prolate spheroidal coordinates (η, ξ, ϕ) are shown in Fig. 5.1. $\boldsymbol{u}_\eta$, $\boldsymbol{u}_\xi$ and $\boldsymbol{u}_\phi$ are the unit vectors oriented in the increasing sense of the respective coordinates. $\xi = \xi_0$ is the equation of the surface of the prolate object. η changes from -1 to +1 while ξ varies from +1 to infinity. c is the semi-focal distance.

The coordinates of the prolate spheroids [1] are related to the rectangular coordinates

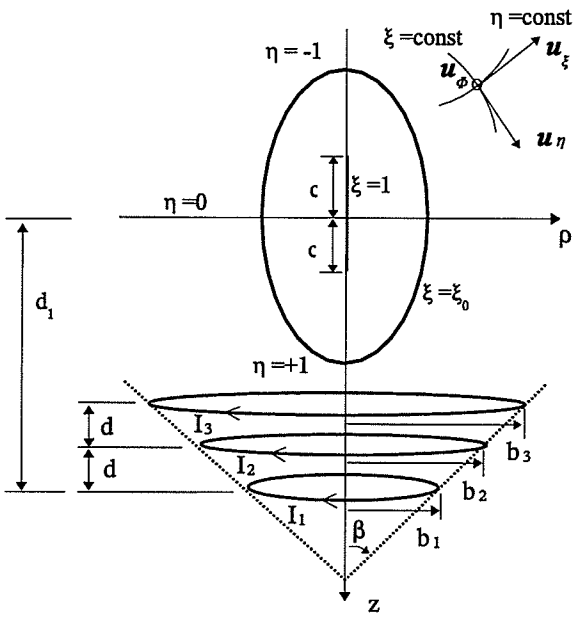

Figure 5.1: Prolate coordinate system.

(x,y,z) by

$$\begin{aligned} x &= c\sqrt{(1-\eta^2)(\xi^2-1)}\cos\phi \\ y &= c\sqrt{(1-\eta^2)(\xi^2-1)}\sin\phi \\ z &= c\eta\xi \end{aligned} \tag{5.1}$$

The corresponding Lamé parameters are

$$h_\eta = c\left(\frac{\xi^2-\eta^2}{1-\eta^2}\right)^{1/2} \qquad h_\xi = c\left(\frac{\xi^2-\eta^2}{\xi^2-1}\right)^{1/2} \qquad h_\phi = c\sqrt{(1-\eta^2)(\xi^2-1)}. \tag{5.2}$$

The semifocul length c is equal to $\sqrt{a_0^2-b_0^2}$ where a_0, b_0 are the semi-major axis and the semi-minor axis, respectively.

5.2 Electric and Magnetic Fields Produced by a Single Turn in Prolate Spheroidal Coordinates

Consider a single turn carrying a sinusoidal current I, whose coordinates are $\eta = \eta_s$ and $\xi = \xi_s$. From(5.1), it is obvious that the radius of the turn b_s is equal to $c\sqrt{(1-\eta_s^2)(\xi_s^2-1)}$. The quasistationary electric and magnetic fields are found at the observation point P in the x-z plane having coordinates $(\eta_p, \xi_p, 0)$. The vector length element of the circular turn at a point (η_s, ξ_s, ϕ') is given by $d\boldsymbol{l}' = -b_s \sin\phi' d\phi' \boldsymbol{u}_x + b_s \cos\phi' d\phi' \boldsymbol{u}_y$, with $dl' = b_s d\phi'$. The position vector of the observation point is expressed as $\boldsymbol{r} = x(\eta_p, \xi_p, 0)\boldsymbol{u}_x + y(\eta_p, \xi_p, 0)\boldsymbol{u}_y + z(\eta_p, \xi_P, 0)\boldsymbol{u}_z$ where functions x, y and z are (see 5.1)

$$x(\eta_p, \xi_p, 0) = c\sqrt{(1-\eta_p^2)(\xi_p^2-1)}$$

$$y(\eta_p, \xi_p, 0) = 0$$

$$z(\eta_p, \xi_p, 0) = c\eta_p\xi_p.$$

The position vector of the source point $\boldsymbol{r}' = b_s\cos\phi'\boldsymbol{u}_x + b_s\sin\phi'\boldsymbol{u}_y + z'(\eta_s, \xi_s, \phi')\boldsymbol{u}_z$. The distance from the source point to the observation point $R = |\boldsymbol{r} - \boldsymbol{r}'|$, is given by

$$R = \sqrt{[x(\eta_p, \xi_p, 0) - b_s\cos\phi']^2 + b_s^2\sin^2\phi' + [z(\eta_p, \xi_p, 0) - z'(\eta_s, \xi_s, \phi')]^2}. \tag{5.3}$$

The substitution of R and $d\boldsymbol{l}'$ into (2.13) yields the vector potential. The tangential electric field intensity E_ϕ is found using (2.9). It is evaluated numerically by discretizing the turn into L elements as given in (5.4),

$$E_\phi = -\frac{j\omega\mu_0 I}{2L}\sum_{i=1}^{L}\frac{b_s\cos\phi_i}{\sqrt{[x(\eta_p, \xi_p, 0) - b_s\cos\phi_i]^2 + b_s^2\sin^2\phi_i + [z(\eta_p, \xi_p, 0) - z'(\eta_s, \xi_s, \phi_i)]^2}} \tag{5.4}$$

where $\phi_i = \frac{2\pi}{L}(i-1)$. The above equation is modified to determine E_ϕ produced by a circular strip whose coordinates of its center line are η_s and ξ_s. The width of the strip is $h_{\eta_s}\Delta\eta_s$, $\Delta\eta_s$ being the incremental η of the strip. It is assumed that the current density is concentrated

on the center line of the strip. The result is

$$E_\phi = -\frac{j\omega\mu_0 J_s h_{\eta_s}\Delta\eta_s}{2L}\cdot \sum_{i=1}^{L}\frac{b_s\cos\phi_i}{\sqrt{[x(\eta_p,\xi_p,0)-b_s\cos\phi_i]^2+b_s^2\sin^2\phi_i+[z(\eta_p,\xi_p,0)-z'(\eta_s,\xi_s,\phi_i)]^2}} \tag{5.5}$$

An expression for the magnetic flux density $\boldsymbol{B}$ is obtained substituting R and $d\boldsymbol{l}'\times\boldsymbol{R}$ into (2.14). In order to evaluate $\boldsymbol{B}$ numerically we discretize the turn into a number of L elements and, then,

$$\begin{aligned}\boldsymbol{B}(\eta_p,\xi_p,0) =& \frac{\mu_0 I b_s}{2L}\sum_{i=1}^{L}\frac{1}{R_i^3}\left[\left\{z(\eta_p,\xi_p,0)-z'(\eta_s,\xi_s,\phi_i)\right\}\cos\phi_i\boldsymbol{u}_x\right.\\ &\left.+\left\{b_s-x(\eta_p,\xi_p,0)\cos\phi_i\right\}\boldsymbol{u}_z\right]\end{aligned} \tag{5.6}$$

where $R_i=\sqrt{[x(\eta_p,\xi_p,0)-b_s\cos\phi_i]^2+b_s^2\sin^2\phi_i+[z(\eta_p,\xi_p,0)-z'(\eta_s,\xi_s,\phi_i)]^2}$. The η-directed component of $\boldsymbol{B}$ is obtained by taking the dot product of (5.6) with the unit vector $\boldsymbol{u}_\eta$. $\boldsymbol{u}_\eta\cdot\boldsymbol{u}_x$, $\boldsymbol{u}_\eta\cdot\boldsymbol{u}_y$ and $\boldsymbol{u}_\eta\cdot\boldsymbol{u}_z$ are listed in Appendix B. Hence, η-directed component is

$$\begin{aligned}B_\eta(\eta_p,\xi_p,0) =& \frac{\mu_0 I b_s}{2L}\sum_{i=1}^{L}\frac{1}{R_i^3}\left[-\eta_p\sqrt{\frac{\xi_p^2-1}{\xi_p^2-\eta_p^2}}\left\{z(\eta_p,\xi_p,0)-z'(\eta_s,\xi_s,\phi_i)\right\}\cos\phi_i\right.\\ &\left.+\xi_p\sqrt{\frac{1-\eta_p^2}{\xi_p^2-\eta_p^2}}\left\{b_s-x(\eta_p,\xi_p,0)\cos\phi_i\right\}\right].\end{aligned} \tag{5.7}$$

Equation (5.7) can be easily modified to determine B_η produced by a circular current-carrying strip assuming the current density is concentrated on its center line.

5.3 Formulation in Prolate Spheroidal Coordinates

The prolate spheroidal coordinate system is used to formulate the integral equations for prolate spheroidal conductors in the presence of a quasistationary magnetic field produced by coaxial turns carrying sinusoidal currents I, as shown in Fig. 5.1.

The ϕ-directed tangential electric field intensity at the conductor surface is the sum of the electric fields produced by the inducing turns and the induced currents on the conductor

itself. Using (2.9), (2.12) and (2.13) the total tangential electric field intensity is obtained as

$$E_\phi = -\frac{j\omega\mu_0}{4\pi}\Bigg[\boldsymbol{u}_\phi \cdot \int_{-1}^{1}\int_{0}^{2\pi} \frac{\boldsymbol{J}_s(\eta')c^2\sqrt{(\xi_0^2-\eta'^2)(\xi_0^2-1)}d\phi' d\eta'}{R_1} + \sum_{k=1}^{N} I_k \int_0^{2\pi} \frac{c\sqrt{(1-\eta_k^2)(\xi_k^2-1)}\cos\phi' d\phi'}{R_k}\Bigg] \tag{5.8}$$

where R_1 is the distance between a source point on a conductor surface and the observation point in the x-z plane on the conductor surface, R_k is the distance between a source point on the k-th turn and the observation point on the conductor. R_1 and R_k are evaluated using (5.3). Using (2.14) and (2.15), the tangential magnetic field intensity is expressed as

$$H_\eta = \frac{1}{4\pi}\Bigg[\boldsymbol{u}_\eta \cdot \int_{-1}^{1}\int_{0}^{2\pi} \frac{J_s(\eta')(\boldsymbol{u}_\phi(\phi')\times\boldsymbol{R}_1)c^2\sqrt{(\xi_0^2-\eta'^2)(\xi_0^2-1)}d\phi' d\eta'}{R_1^3} + \sum_{k=1}^{N} I_k \boldsymbol{u}_\eta \cdot \int_0^{2\pi} \frac{(\boldsymbol{u}_\phi(\phi')\times\boldsymbol{R}_k)c\sqrt{(1-\eta_k^2)(\xi_k^2-1)}d\phi'}{R_k^3}\Bigg]. \tag{5.9}$$

The relation between E_ϕ and H_η is

$$\frac{E_\phi}{H_\eta} = -Z_s(\eta). \tag{5.10}$$

In the case of the simplest SI integral equations, $Z_s(\eta)$ is equal to the standard surface impedance, Z_s. The MSI integral equations are formed by taking $Z_s(\eta) = Z_{smod}$, where the evaluation of the modified Z_{smod} is given in section 5.5. As already mentioned, the integral equation based on the PC model is obtained forcing E_ϕ to be null on the conductor surface.

5.4 Solution of Integral Equations in Prolate Coordinates

Integral equations are solved by applying the point matching procedure and converting them into a set of linear equations, $[l_{nm}][J_n] = [g_n]$. The rectangular single pulse function and the

Dirac delta function are chosen as the basis function and the weighting function, respectively. This means that the current distribution on the spheroid surface is approximated by M coaxial circular strips, each carrying a uniformly distributed current [6]. The integral equation in (5.10) is transformed into a linear equation with M number of unknowns, using (5.4), (5.5) and (5.7). The matrix element l_{nm} is given as

$$\begin{aligned} l_{nm}|_{n\neq m} = &- \frac{j\omega\mu_0 c^2 \Delta\eta_m}{2L} \sum_{i=1}^{L} \frac{\sqrt{(\xi_0^2-\eta_m^2)(\xi_0^2-1)}\cos\phi_i}{R_{mi}} \\ &\frac{Z_s(\eta_n) c^2 \Delta\eta_m}{2L} \sum_{i=1}^{L} \frac{1}{R_{mi}^3} \Bigg[-\eta_n(\xi_0^2-1)\sqrt{\frac{\xi_0^2-\eta_m^2}{\xi_0^2-\eta_n^2}} \Big\{ c\eta_n\xi_0 - c\eta_m\xi_0 \Big\} \cos\phi_i \\ &+ c\xi_0(\xi_0^2-1)\sqrt{(\xi_0^2-\eta_m^2)}\sqrt{\frac{1-\eta_n^2}{\xi_0^2-\eta_n^2}} \Big\{ \sqrt{1-\eta_m^2} - \sqrt{1-\eta_n^2}\cos\phi_i \Big\} \Bigg] \end{aligned} \tag{5.11}$$

where R_{mi} is the distance from the center of the i-th element on the m-th strip to the observation point on the n-th strip. g_n is (see 5.12).

$$\begin{aligned} g_n = &\frac{j\omega\mu_0 c}{2L} \sum_{k=1}^{N} I_k \sum_{i=1}^{L} \frac{\sqrt{(1-\eta_k^2)(\xi_k^2-1)}\cos\phi_i}{R_{ki}} \\ &- \frac{c^2 Z_s(\eta_n)}{2L} \sum_{k=1}^{N} I_k \sqrt{(1-\eta_k^2)(\xi_k^2-1)} \sum_{i=1}^{L} \frac{1}{R_{ki}^3} \Bigg[-\eta_n \sqrt{\frac{\xi_0^2-1}{\xi_0^2-\eta_n^2}} \Big\{ \eta_n\xi_0 - \eta_k\xi_k \Big\} \cos\phi_i \\ &+ \xi_0 \sqrt{\frac{1-\eta_n^2}{\xi_0^2-\eta_n^2}} \Big\{ \sqrt{(1-\eta_k^2)(\xi_k^2-1)} - \sqrt{(1-\eta_n^2)(\xi_0^2-1)}\cos\phi_i \Big\} \Bigg] \end{aligned} \tag{5.12}$$

where R_{ki} is the distance from the center of the i-th element on the k-th turn to the observation point. l_{nn} is evaluated treating the singularities by using (3.12) and (3.13). All elements in $[l_{nm}]$ and $[g_n]$ are found by enforcing $E_\phi/H_\eta = -Z_s(\eta)$ at the center line of each strip on the conductor.

The prolate spheroid is discretized into circular strips such that the incremental η for each strip, $\Delta\eta$, is the same for each strip. Then the width of the strips ($h_\eta\Delta\eta$) closer to poles is wider than that of the strips closer to the equator. The results obtained discretizing the surface into strips with same $\Delta\eta$ are not accurate especially for the SI integral equation. This

is why the conductor surface is discretized into strips with same width. The coordinates of the center line of the m-th strip, η_m, is calculated using (5.13) where strips are counted starting from the pole corresponding to $\eta = -1$.

$$\int_{-1}^{\eta_m} h_\eta d\eta = \frac{(m - 0.5) \int_{-1}^{1} h_\eta d\eta}{M} \tag{5.13}$$

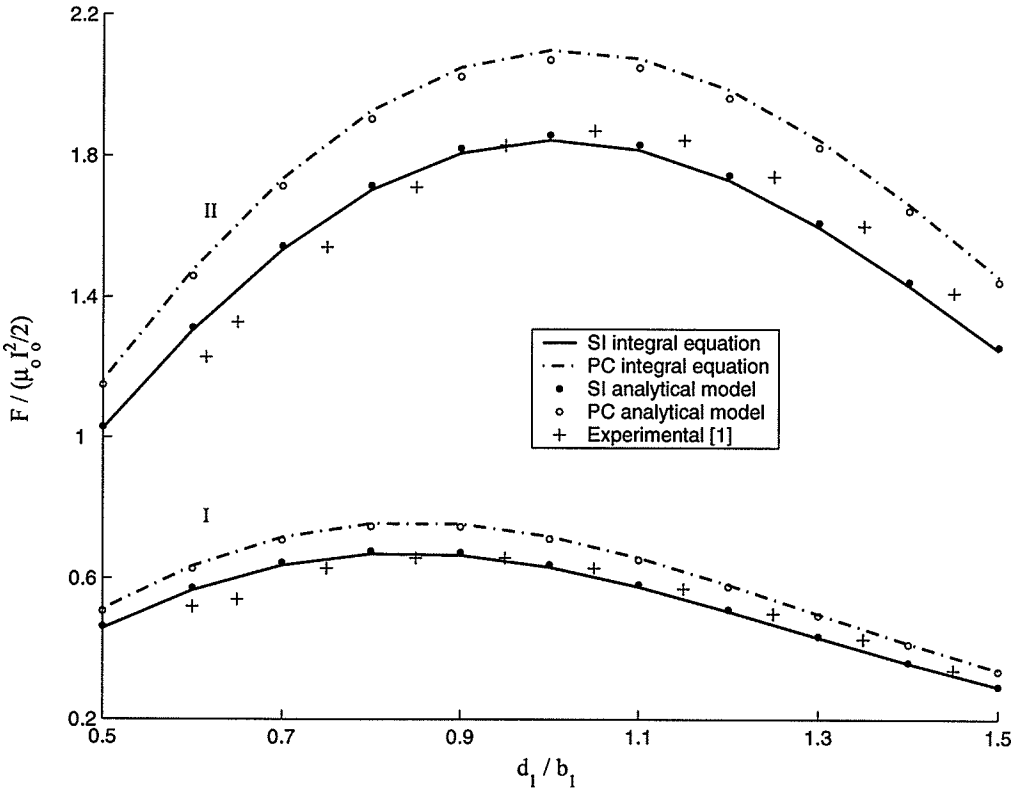

Figure 5.2: Normalized force versus d_1/b_1 for aluminum prolate spheroids at 2 kHz, with $N = 3$, $\tan\beta = 0.4$, $d/b_1 = 0.25$, $b_0/a_0 = 0.6$, and $b_0 = 2$ cm: (I)$b_0/b_1 = 0.5$; (II)$b_0/b_1 = 0.75$.

Numerical results both from the PC integral equation and the SI integral equation are generated for prolate spheroids of major and minor semi axis a_0 and b_0, respectively, in the presence of three coaxial turns connected in series and carrying a current I_0. The three turns are placed on the surface of a cone of opening 2β, as shown in Fig.5.1, the distance between the plane of the lower turn and the spheroid center being d_1. Power loss in the prolate conductor

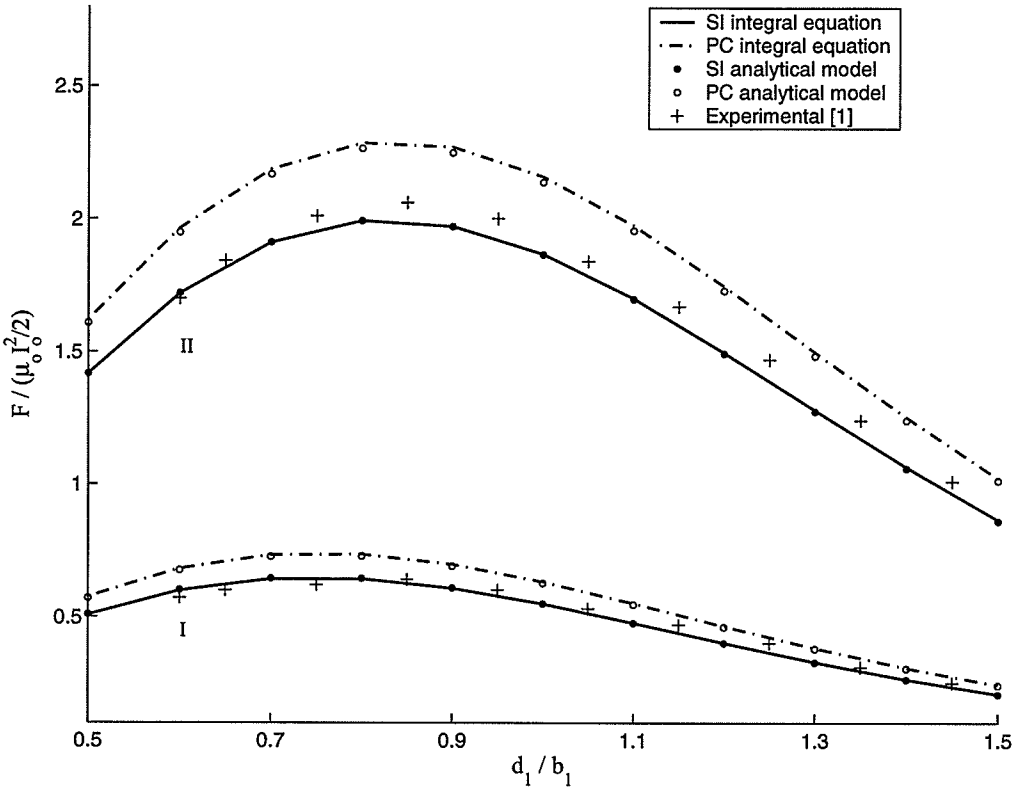

Figure 5.3: Normalized force versus d_1/b_1 for aluminum prolate spheroids at 2 kHz, with $N = 3$, $\tan\beta = 0.4$, $d/b_1 = 0.25$, $b_0/a_0 = 0.8$, and $b_0 = 2$ cm: (I)$b_0/b_1 = 0.5$; (II)$b_0/b_1 = 0.75$.

and the electromagnetic force upon it are evaluated using (3.16) and (3.17).

The time-average force for prolate spheroids at a frequency of 2 kHz, with $N = 3$, $\tan\beta = 0.4$, $d/b_1 = 0.25$, $b_0 = 2$ cm, with $b_0/b_1 = 0.5, 0.75$ and $b_0/a_0 = 0.6, 0.8$ is plotted in Figs. 5.2 and 5.3, respectively. The force obtained from the SI and PC integral equations is in good agreement with that from the analytical solutions for the SI and PC models. As expected, the experimental data are much closer to the results obtained from the SI integral equation. The accuracy of the numerical results for the force has been increased by increasing the number M of strips up to 20 and the number of strip elements on each inducing turn up to 40. In Fig. 5.4, the normalized force has been plotted for a frequency of 8 kHz, with $N = 3$, $\tan\beta = 0.4$, $d/b_1 = 0.25$, $b_0 = 2$ cm with $b_0/b_1 = 0.5$ for $b_0/a_0 = 0.4$ and 0.6. The depth of penetration

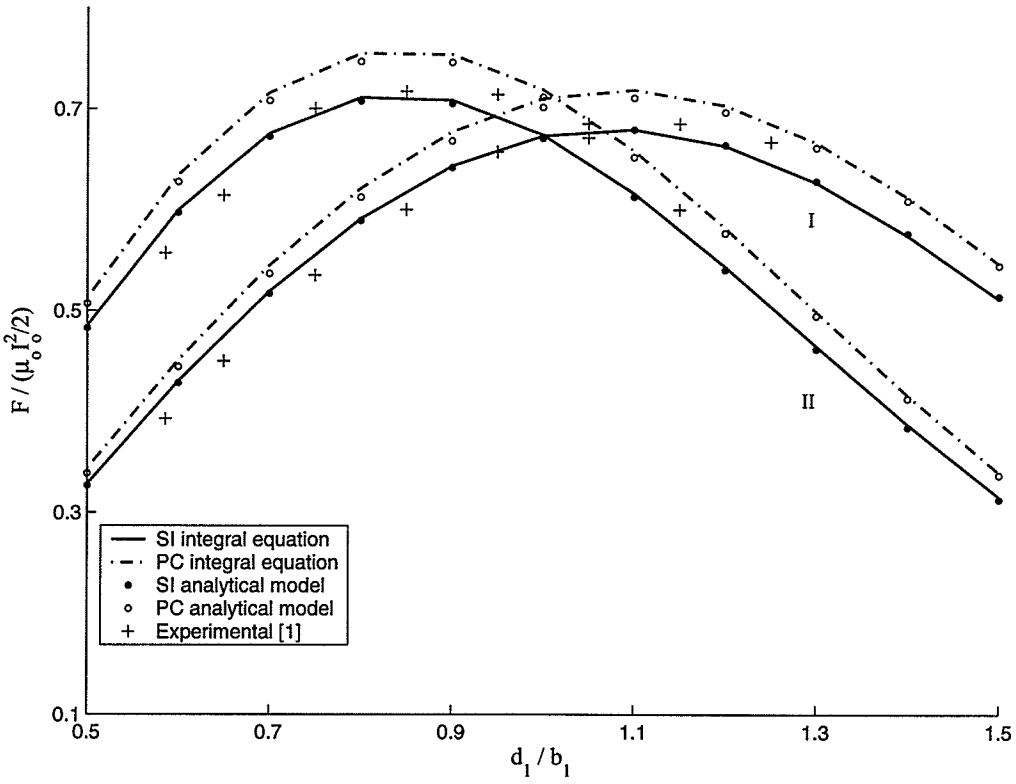

Figure 5.4: Normalized force versus d_1/b_1 for aluminum prolate spheroids at 2 kHz, with $N = 3$, $\tan\beta = 0.4$, $d/b_1 = 0.25$, $b_0/b_1 = 0.5$, and $b_0 = 2$ cm: (I)$b_0/a_0 = 0.4$; (II)$b_0/a_0 = 0.6$.

for aluminium at the frequency of 2 kHz is about 1.8 mm. When the frequency has been increased, the deviation of the PC model results from the experimental data and from the SI model results has decreased.

The errors associated with the electric and magnetic fields at the observation point produced by the neighboring current-carrying strips are minimized by dividing the circular strips into 10 sub-strips. Each sub-strip on the m-th strip has the same current density J_m. The total contribution from the m-th strip is evaluated by summing up the individual contributions of the sub-strips on the m-th strip, as described in chapter 4. Table 5.1 compares the normalized power loss obtained from solving the PC integral equations using a fine mesh and a coarse mesh. The surface has been discretized into 30 strips and each strip into 60 elements

for the coarse mesh. Analytical results are also given for a frequency of 8 kHz, with $N = 3$, $\tan\beta = 0.4$, $d/b_1 = 0.25$, $b_0 = 2$ cm, $b_0/b_1 = 0.5$, $d_1/b_1 = 1$ with $b_0/a_0 = 0.1, 0.5$ and 0.9. It is evident that the results obtained with a fine mesh are much closer to the analytical results than results obtained with a coarse mesh as expected.

Table 5.1: Comparison of power loss obtained from PC integral equations with a fine mesh and a coarse mesh for prolate spheroids at 8 kHz, with $N = 3$, $\tan\beta = 0.4$, $d/b_1 = 0.25$, $b_0 = 2$ cm, $b_0/b_1 = 0.5$, $d_1/b_1 = 1$.

b_0/a_0	coarse mesh	fine mesh	Analytical results from PC model [1]
0.1	7.8042	9.9619	9.7680
0.5	8.344	8.2948	8.2339
0.9	6.7736	6.6537	6.6538

Galerkin's method has also been implemented, by choosing both the basis functions and weighting functions to be three constrained rectangular pulses. The accuracy of the numerical results obtained from Galerkin's method is higher. Namely, the number of basis functions consisting of one rectangular pulse required to achieve the same accuracy has to be increased to about twice the number of basis functions consisting of three constrained rectangular pulses for spheroids with the same axial ratios between 0.4 and 0.8.

5.5 Modified Surface Impedance for Prolate Spheroids

The surface impedance of the prolate conductor is modified using (2.34). ϕ and η are the principal curvature coordinates for a prolate spheroid and ϕ and η are equivalent to w and v in section 2.2. The curvature k_η is determined by using its definition [3], [16],

$$k_\eta = \frac{\xi_0\sqrt{\xi_0^2 - 1}}{c[\xi_0^2 - \eta^2]^{3/2}}. \tag{5.14}$$

Then the curvature $k_\phi = \xi/\{c\sqrt{(\xi_0^2-\eta^2)(\xi^2-1)}\}$.Substituting k_η and k_ϕ into (2.35), the modified surface impedance is evaluated as $Z_{smod} = (1-p)Z_s$.

We have considered spheroids with various axial ratios, $b_0/a_0 = 0.4; 0.6; 0.8$ at a frequency of 8 kHz, with $N = 3$, $\tan\beta = 0.4$, $d/b_1 = 0.25$, $b_0/b_1 = 0.5$, $d_1/b_1 = 1$, and $b_0 = 2$ cm. Numerical results for the force from both the MSI integral equations and SI integral equations are shown in Table 5.2. Experimental results are much closer to results from the MSI integral equation than those from the SI integral equations.

Table 5.2: Normalized force evaluated from SI and MSI models at a frequency of 8 kHz with $N = 3$, $\tan\beta = 0.4$, $d/b_1 = 0.25$, $b_0/b_1 = 0.5$, $d_1/b_1 = 1$, and $b_0 = 2$ cm.

b_0/a_0	Using Z_s	Using Z_{smod}	Experimental [1]
0.4	0.6706	0.6712	0.6714
0.6	0.6728	0.6734	0.6928
0.8	0.5891	0.5894	0.6214

Chapter 6

Integral Equations for Oblate Spheroids

In this chapter, we formulate integral equations for oblate spheroids in the presence of current-carrying turns. The system of curvilinear coordinates of the oblate spheroid is chosen for this formulation.

The oblate spheroidal coordinate system is discussed in section 6.1. The electric and magnetic field intensities produced by a current-carrying turn are found in oblate spheroidal coordinates and numerical results from the PC integral equations and the SI integral equations are compared with relevant analytical results.

6.1 Oblate Spheroidal Coordinates

In oblate spheroidal coordinates (η, ξ, ϕ), the range of ξ is from 0 to infinity and the unit vectors are $\boldsymbol{u}_\eta$, $\boldsymbol{u}_\xi$ and $\boldsymbol{u}_\phi$ as shown in Fig. 6.1. The surface of an oblate spheroid is given by the equation $\xi = \xi_0$. c is again the semi-focal length.

Oblate coordinates are related to rectangular coordinates by

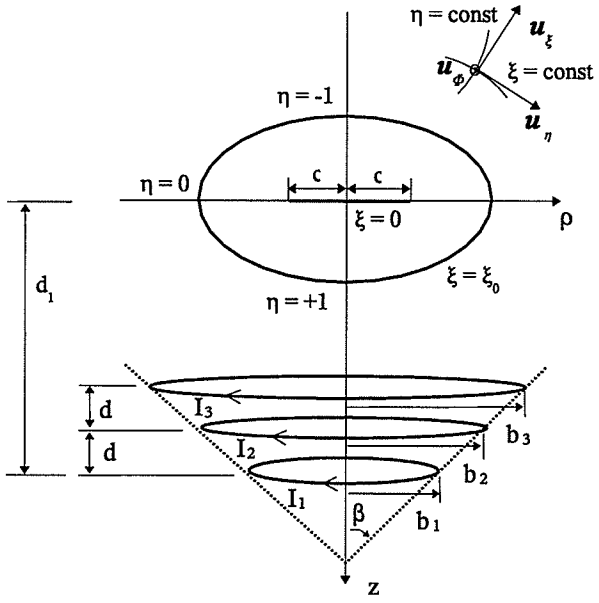

Figure 6.1: Oblate coordinate system.

$$
\begin{aligned}
x &= c\sqrt{(1-\eta^2)(\xi^2+1)}\cos\phi \\
y &= c\sqrt{(1-\eta^2)(\xi^2+1)}\sin\phi \\
z &= c\eta\xi,
\end{aligned}
\tag{6.1}
$$

where the corresponding Lamé parameters are

$$
h_\eta = c\left(\frac{\xi^2+\eta^2}{1-\eta^2}\right)^{1/2} \qquad h_\xi = c\left(\frac{\xi^2+\eta^2}{\xi^2-1}\right)^{1/2} \qquad h_\phi = c\sqrt{(1-\eta^2)(\xi^2+1)}. \tag{6.2}
$$

c is equal to $\sqrt{b_0^2 - a_0^2}$ where a_0 and b_0 are the semi-minor and the semi-major axes, respectively.

A turn carrying a sinusoidal current I, whose coordinates are η_s and ξ_s, has a radius $b_s = c\sqrt{(1-\eta_s^2)(\xi_s^2+1)}$. The electric field intensity and magnetic flux density produced by the turn are calculated at the observation point (η_p, ξ_p,0) in the x-z plane. The position vector of the observation point is given by $\boldsymbol{r} = x(\eta_p, \xi_p, 0)\boldsymbol{u}_x + y(\eta_p, \xi_p, 0)\boldsymbol{u}_y + z(\eta_p, \xi_p, 0)\boldsymbol{u}_z$ where

$$x(\eta_p, \xi_p, 0) = c\sqrt{(1-\eta_p^2)(\xi_p^2+1)}$$

$$y(\eta_p, \xi_p, 0) = 0$$

$$z(\eta_p, \xi_p, 0) = c\eta_p\xi_p.$$

The position vector of the source point is $\boldsymbol{r'} = b_s\cos\phi'\boldsymbol{u}_x + b_s\sin\phi'\boldsymbol{u}_y + z'(\eta_s, \xi_s, \phi')\boldsymbol{u}_z$. The vector element of the turn is $d\boldsymbol{l'} = -b_s\sin\phi' d\phi'\boldsymbol{u}_x + b_s\cos\phi' d\phi'\boldsymbol{u}_y$. The distance between the source point and the observation point is

$$R = \sqrt{[x(\eta_p, \xi_p, 0) - b_s\cos\phi']^2 + b_s^2\sin^2\phi' + [z(\eta_p, \xi_p, 0) - z'(\eta_s, \xi_s, \phi')]^2}. \tag{6.3}$$

Substitution of R and $d\boldsymbol{l'}$ into (2.13) yields an expression for the vector potential produced by the turn. An equation for the tangential electric field intensity E_ϕ is found using (2.9). The turn is discretized into L elements. E_ϕ is evaluated numerically from an equation similar to (5.4). Modifying this equation as in (5.5), the tangential electric field produced by a current carrying-strip, whose center line has the coordinates η_s, ξ_s is computed numerically. The distance vector from a point on the turn to the point P is

$$\boldsymbol{R} = [x(\eta_p, \xi_p, 0) - b_s\cos\phi']\boldsymbol{u}_x - b_s\sin\phi'\boldsymbol{u}_y + [z(\eta_p, \xi_p, 0) - z'(\eta_s, \xi_s, \phi')]\boldsymbol{u}_z. \tag{6.4}$$

We obtain an expression for the magnetic flux density at P substituting $\boldsymbol{R}$ and $d\boldsymbol{l'} \times \boldsymbol{R}$ into (2.14). An equation similar to (5.6) is obtained for the flux density. The tangential component of the magnetic flux density is obtained by using (A.10), (A.11) and (A.12) as

$$\begin{aligned} B_\eta(\eta_p, \xi_p, 0) = \frac{\mu_0 I b_s}{2L}\sum_{i=1}^{L}\frac{1}{R_i^3}\Bigg[&-\eta_p\sqrt{\frac{\xi_p^2+1}{\xi_p^2+\eta_p^2}}\Big\{z(\eta_p, \xi_p, 0) - z'(\eta_s, \xi_s, \phi_i)\Big\}\cos\phi_i \\ &+\xi_p\sqrt{\frac{1-\eta_p^2}{\xi_p^2+\eta_p^2}}\Big\{b_s - x(\eta_p, \xi_p, 0)\cos\phi_i\Big\}\Bigg]. \end{aligned} \tag{6.5}$$

B_η produced by a strip carrying an uniform current density, whose coordinates of the center line are η_s and ξ_s, is evaluated by replacing I in (6.5) with $J_s h_{\eta_s}\Delta\eta_s$, where J_s and $h_{\eta_s}\Delta\eta_s$ are

the current density on the strip and the width of the strip, respectively. $\Delta\eta_s$ is the incremental η for the strip s.

6.2 Formulation of Integral Equations in Oblate Coordinates

Integral equations are now formulated for a oblate spheroidal conductor in the presence of a quasistationary magnetic field produced by sinusoidal current-carrying coaxial turns, as shown in Fig. 6.1. Currents flowing in ϕ-direction is induced on the conductor.

The total tangential electric field intensity at the conductor surface produced by the inducing turns and the induced currents is found using (2.9), (2.12) and (2.13), namely,

$$E_\phi = -\frac{j\omega\mu_0}{4\pi}\left[\boldsymbol{u}_\phi \cdot \int_{-1}^{1}\int_{0}^{2\pi} \frac{\boldsymbol{J}_s c^2\sqrt{(\xi_0^2+\eta^2)(\xi_0^2+1)}d\phi' d\eta'}{R_1} + \sum_{k=1}^{N} I_k \int_0^{2\pi} \frac{c\sqrt{(1-\eta_k^2)(\xi_k^2+1)}\cos\phi' d\phi'}{R_k}\right] \tag{6.6}$$

where R_1 is the distance between a source point on the conductor surface and the observation point, and R_k is the distance between a source point on the k-th turn and the observation point. R_1 and R_k are expressed using (6.3). The total tangential magnetic field intensity is obtained in the form

$$H_\eta = \frac{1}{4\pi}\left[\boldsymbol{u}_\eta \cdot \int_{-1}^{1}\int_{0}^{2\pi} \frac{\boldsymbol{J}_s\{\boldsymbol{u}_\phi(\phi')\times\boldsymbol{R}_1\}c^2\sqrt{(\xi_0^2+\eta^2)(\xi_0^2+1)}d\phi' d\eta'}{R_1^3} + \sum_{k=1}^{N} I_k \boldsymbol{u}_\eta \cdot \int_0^{2\pi} \frac{\{\boldsymbol{u}_\phi(\phi')\times\boldsymbol{R}_k\}c\sqrt{(1-\eta_k^2)(\xi_k^2+1)}d\phi'}{R_k^3}\right]. \tag{6.7}$$

The integral equation is formulated relating E_ϕ and H_η through

$$\frac{E_\phi}{H_\eta} = -Z_s(\eta). \tag{6.8}$$

The PC integral equation is obtained forcing E_ϕ to be zero. The SI integral equation is formed with $Z_s(\eta) = Z_s$ and the MSI integral equation is obtained taking $Z_s(\eta) = Z_{smod}$, where Z_{smod} is given in section 6.3.1.

6.3 Numerical Results for Oblate Spheroids

A point matching procedure is again employed to evaluate numerically the unknown current density. The conductor surface is discretized into M circular coaxial strips, each carrying a current of density J_m. The total tangential electric or magnetic field intensity at a point on a strip is obtained from the contributions of all the strips and of the inducing turns. These contributions are evaluated as elaborated in section 6.1. A set of linear algebraic equations, $[l_{nm}][J_m] = [g_n]$ is obtained by satisfying (6.8) at discrete points on the surface. The matrix element l_{nm} is found to be

$$\begin{aligned} l_{nm}|_{n\neq m} = &- \frac{j\omega\mu_0 c^2 \Delta\eta_m}{2L} \sum_{i=1}^{L} \frac{\sqrt{(\xi_0^2+\eta_m^2)(\xi_0^2+1)}\cos\phi_i}{R_{mi}} + \frac{Z_s(\eta_n) c^2 \Delta\eta_m}{2L} \sum_{i=1}^{L} \frac{1}{R_{mi}^3} \Bigg[\\ &- \frac{\eta_n(\xi_0^2+1)\sqrt{\xi_0^2+\eta_m^2}}{\sqrt{\xi_0^2+\eta_n^2}} \Big\{ c\eta_n\xi_0 - c\eta_m\xi_0 \Big\} \cos\phi_i \\ &+ \frac{c\xi_0(\xi_0^2+1)\sqrt{1-\eta_n^2}\sqrt{(\xi_0^2+\eta_m^2)}}{\sqrt{\xi_0^2+\eta_n^2}} \Big\{ \sqrt{1-\eta_m^2} - \sqrt{1-\eta_n^2}\cos\phi_i \Big\} \Bigg] \end{aligned} \tag{6.9}$$

where R_{mi} is the distance from the center of the i-th element on the m-th strip to the observation point in the x-z plane on the n-th strip. g_n is expressed as

$$\begin{aligned} g_n = &j\frac{\omega\mu_0 c}{2L} \sum_{k=1}^{N} I_k \sum_{i=1}^{L} \frac{\sqrt{(1-\eta_k^2)(\xi_0^2+1)}\cos\phi_i}{R_{ki}} \\ &- \frac{c^2 Z_s(\eta_n)}{2L} \sum_{k=1}^{N} I_k \sqrt{(1-\eta_k^2)(\xi_k^2+1)} \sum_{i=1}^{L} \frac{1}{R_{ki}^3} \Bigg[-\eta_n \sqrt{\frac{\xi_0^2+1}{\xi_0^2+\eta_n^2}} \Big\{ \eta_n\xi_0 - \eta_k\xi_k \Big\} \cos\phi_i \\ &+ \frac{\xi_0\sqrt{1-\eta_n^2}}{\sqrt{\xi_0^2+\eta_n^2}} \Big\{ \sqrt{(1-\eta_k^2)(\xi_k^2+1)} - \sqrt{(1-\eta_n^2)(\xi_0^2+1)}\cos\phi_i \Big\} \Bigg] \end{aligned} \tag{6.10}$$

where R_{ki} is the distance from the center of the i-th element on the k-th turn to the observation point on the n-th strip. The diagonal element l_{nn} is evaluated using (3.12) and (3.13), as

described in chapter 3. When the conductor surface is divided into strips such that $\Delta\eta_m$ is the same for all of them, the width of the strips closer to the poles are higher than that of the strips near to the equator as in the case of prolate spheroids. In order to improve the accuracy of the results, the conductor surface is divided into strips of equal width using (5.13).

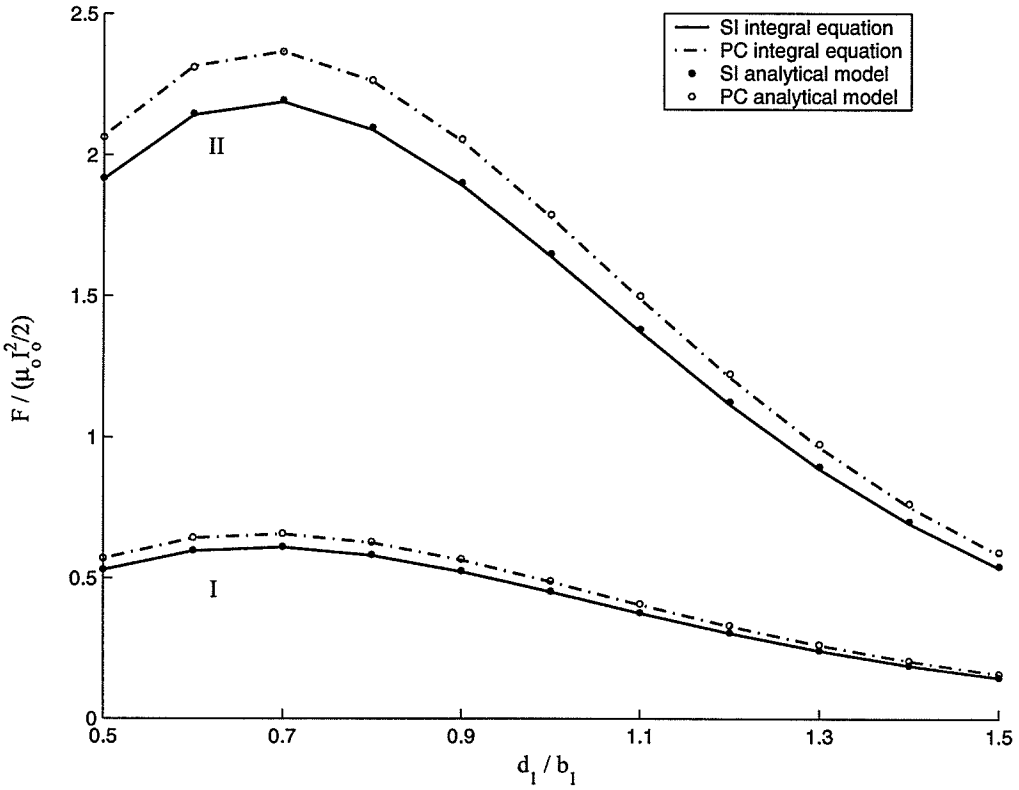

Figure 6.2: Normalized force versus d_1/b_1 for aluminum oblate spheroids at 8 kHz, with $N = 3$, $\tan\beta = 0.4$, $d/b_1 = 0.25$, $b_0/a_0 = 1.25$ and $b_0 = 2$ cm: (I) $b_0/b_1 = 0.5$; (II) $b_0/b_1 = 0.75$.

Numerical results are generated from both the SI integral equations and PC integral equations for oblate spheroids of minor and major semi-axes a_0 and b_0, respectively, in the presence of the magnetic field produced by a system of three coaxial turns connected in series and carrying a current I_0. The turns are placed as shown in Fig. 6.1. The distance between the plane of the lower turn and the spheroid center is d_1. The power loss and the electromagnetic force upon oblate spheroids are computed using (3.15) and (3.16).

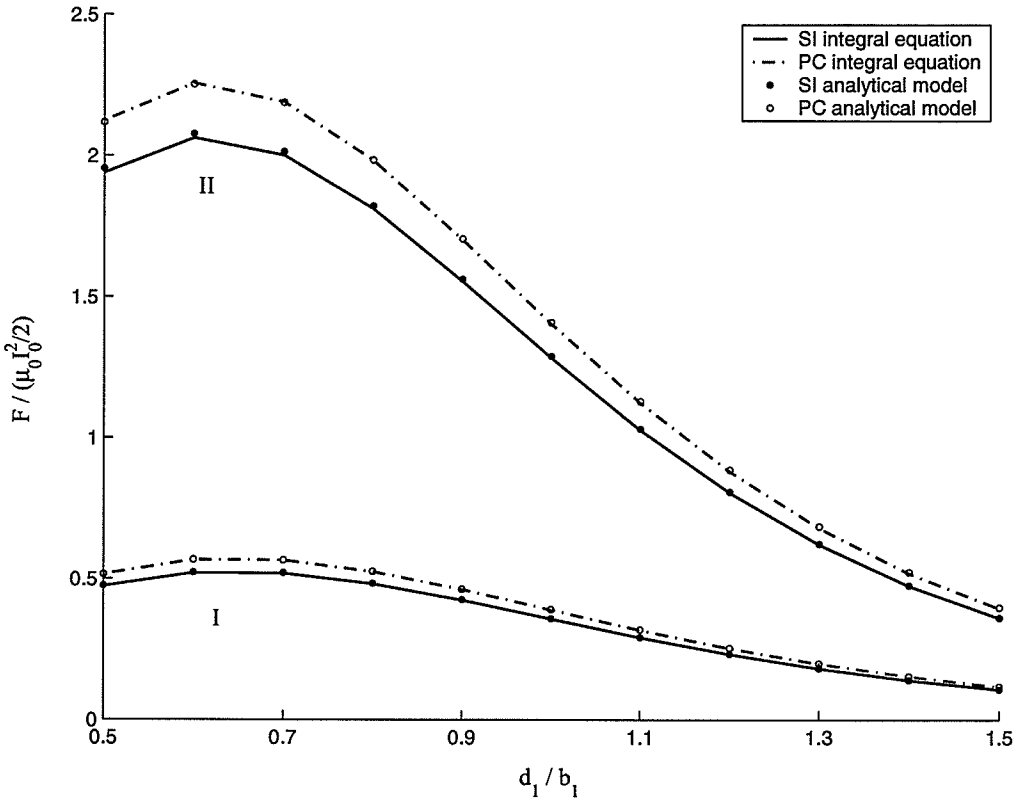

Figure 6.3: Normalized force versus d_1/b_1 for aluminum oblate spheroids at 8 kHz, with $N = 3$, $\tan\beta = 0.4$, $d/b_1 = 0.25$, $b_0/a_0 = 2$ and $b_0 = 2$ cm: (I) $b_0/b_1 = 0.5$; (II) $b_0/b_1 = 0.75$.

The time-average force for oblate spheroids at a frequency of 8 kHz, with $N = 3$, $\tan\beta = 0.4$, $d/b_1 = 0.25$, $b_0 = 2$ cm with $b_0/b_1 = 0.5; 0.75$ and $b_0/a_0 = 1.25; 2$ is plotted in Figs. 6.2 and 6.3, respectively. The force obtained from the SI and PC integral equations is in good agreement with that from the analytical solutions for the SI and PC models. The oblate spheroidal surfaces have been discretized in 30 strips and each strip into 60 elements.

Errors which arise due to the fact that the current density is assumed to be concentrated on the center line of the strip are minimized using a fine mesh.Each strip is divided into 10 sub-strips which carry the same current density. The contribution to E_ϕ and H_η at the observation point by the m-th strip is found by adding up individual contributions from the

sub-strips on the m-th strip. Table 6.1 compares power loss evaluated using the PC integral equation for oblate spheroids at 8 kHz, with $N = 3$, $\tan\beta = 0.4$, $d/b_1 = 0.25$, $b_0 = 2$ cm and $b_0/b_1 = 0.5$, for different ratios of d_1/b_1 and b_0/a_0. The number of strips is $M = 30$ and each strip has 60 elements. The results obtained with the fine mesh are closer to the analytical solutions.

Table 6.1: Comparison of normalized power loss obtained from PC integral equations with a fine mesh and a coarse mesh for oblate spheroids at 8 kHz, with $N = 3$, $\tan\beta = 0.4$, $d/b_1 = 0.25$, $b_0 = 2$cm.

b_0/a_0	d_1/b_1	Coarse mesh	Fine mesh	Analytical results from PC model
1.25	0.6	6.00	5.93	5.67
	1.2	1.78	1.75	1.55
5	0.6	5.22	5.14	5.11
	1.2	1.31	1.27	1.28

6.3.1 Modified Surface Impedance for Oblate Spheroids

The coordinates ϕ and η are the principal curvature coordinates for oblate spheroids, as in the case of prolate spheroids. The curvature k_ϕ and k_η are [3], [16]

$$k_\phi = \frac{\xi}{\{c\sqrt{(\xi_0^2+\eta^2)(\xi_0^2+1)}\}}, \qquad k_\eta = \frac{\xi_0\sqrt{\xi_0^2+1}}{c[\xi_0^2+\eta^2]^{3/2}}. \tag{6.11}$$

The modified surface impedance, Z_{smod} is equal to $(1-p)Z_s$, where p is found from (2.35).

Table 6.2 compares numerical results obtained from the SI integral equations and the MSI integral equations for the normalized forces upon oblate spheroids at a frequency of 8 kHz, with $N = 3$, $\tan\beta = 0.4$, $d/b_1 = 0.25$, $b_0/b_1 = 0.5$ and $d_1/b_1 = 0.6$ and different b_0/a_0 and b_0. The results show that the influence of the modification of the surface impedance increases

when the dimensions of the spheroids reduce or the ratio b_0/a_0 increases.

Table 6.2: Comparison of normalized force obtained from SI and MSI integral equations for oblate spheroids at 8 kHz with $N = 3$, $\tan\beta = 0.4$, $d/b_1 = 0.25$, $b_0/b_1 = 0.5$ and $d_1/b_1 = 0.6$.

b_0/a_0	b_0 (cm)	SI integral equation	MSI integral equation
1.25	2	0.6006	0.6003
	10	0.6368	0.6368
5	2	0.4103	0.4071
	10	0.4472	0.4470

Chapter 7

Conclusion

Integral equations have been formulated using the PC and the SI models for arbitrarily shaped axisymmetric conductors in the presence of quasistationary electromagnetic fields produced by coaxial turns carrying current sinusoidally varying with time. Numerical results have been generated for spherical conductors, prolate spheroidal conductors, and oblate spheroidal conductors. The surface integrals are taken in principal values and their singularities were evaluated by considering separately the contributions of a rectangular self-patch. A formula was derived to evaluate the electric field intensity at the center of the self-patch. Electromagnetic forces upon conducting bodies considered have been found in a simple manner by evaluating the total force on the inducing turns.

For spherical conductors, integral equations have been formulated employing spherical coordinates. They were solved by applying the point matching and Galerkin's methods. It is noticed that the number of basis functions consisting of one rectangular pulse required to achieve the same accuracy has to be increased to about twice the number of basis functions consisting of three constrained rectangular pulses for the spheres considered. Normalized power loss and force for different spheres were evaluated both from the PC and the SI integral equations at different frequencies, and they were compared with exact analytical results. The power loss obtained from the SI integral equations is closer to the exact analytical solution

than that from the the PC integral equations for spheres with the ratio r_0/δ higher than 20. Errors associated with the power loss computed from the integral equations increase with the decrease of r_0/δ. But the SI integral equation produces more accurate results than the PC integral equation for forces upon spheres even when r_0/δ is less than 20. For the spheres considered, the accuracy has been improved by employing a mesh where neighboring strips to the observation point had been subdivided. The same accuracy can be achieved by doubling the number of strips and the number of elements on each strip, but with increased computing time.

Power loss and electromagnetic force upon prolate spheroids in the the presence of quasi-stationary magnetic fields have been determined by solving both SI and PC integral equations which were formulated in prolate spheroidal coordinates. Normalized forces obtained from the PC and SI models were compared with experimental data for prolate spheroids with different axial ratios and with the ratio of the smallest semi-axis to the depth of penetration being more than 10. The force calculated from the SI integral equations is closer to the experimental data. The normalized power losses for prolate spheroids with axial ratios below 0.2, obtained from the PC integral equation when employing a coarse mesh, deviate significantly from the analytical results obtained by using the PC model. The numerical solution of the integral equation has been improved significantly by employing a finer mesh. Normalized forces evaluated from the MSI integral equations have been compared with those obtained from the SI integral equations for various prolate spheroids. Numerical experiments performed show that the standard SI integral equation is sufficient for many practical applications.

Power loss and electromagnetic force have also been evaluated for oblate spheroids with various axial ratios. They are in good agreement with analytical results. The comparison between the performance of the integral equations based on the SI and PC models allows one

to decide which of the two integral equations is to be used for various engineering applications in terms of the desired accuracy.

7.1 Future Work

Techniques for improving the accuracy of the local quantities evaluated from the SI integral equations for objects with the ratio of the smallest dimension to the depth of penetration below 20 are to be studied further.

We have discretized the conductor surfaces only into rectangular elements. Instead, this discretization can be performed by employing triangular elements which are expected to give better results. The dimension of the elements closer to the poles can be reduced in order to reduce the errors introduced near to poles.

In this dissertation, we have considered only conductors with smooth boundaries. It is important to compare results obtained from the PC and SI integral equations for conductors with sharp edges and vertices.

Appendix A

Electric Field Intensity of a Self-Patch

The electric field intensity, produced by a rectangular current- carrying element, at its center is found analytically. The rectangular patch of dimensions g'-by-h' carries a constant current density J_s as shown in figure A.1. Using (2.12) and (2.9), the electric field intensity at the center of the patch is

$$E' = -\frac{j\omega\mu_0 J_s}{\pi} \int_0^{g'/2} \int_0^{h'/2} \frac{1}{\sqrt{x^2+y^2}} dy dx. \tag{A.1}$$

The direction of E' is in the x-direction. The integral with respect to x is solved according to formula 200.01 in [2] as

$$\begin{aligned} E' &= -\frac{j\omega\mu_0 J_s}{\pi} \int_0^{g'/2} \ln\left(\frac{h'/2+\sqrt{x^2+(h'/2)^2}}{x}\right) dx \\ &= -\frac{j\omega\mu_0 J_s}{\pi} \int_0^{g'/2} \ln\left(\frac{1/x+\sqrt{(2/h')^2+(1/x)^2}}{2/h'}\right) dx \end{aligned} \tag{A.2}$$

We make the substitution $x = 1/z$ and $dx = -(1/z^2)dz$ into (A.2), which yields

$$E' = \frac{j\omega\mu_0 J_s}{\pi} \int_\infty^{2/g'} \frac{1}{z^2} \ln\left(\frac{z+\sqrt{(2/h')^2+z^2}}{2/h'}\right) dz. \tag{A.3}$$

With [2]

$$\ln\left(\frac{x+\sqrt{x^2+a^2}}{a}\right) = \sinh^{-1}\frac{x}{a} \tag{A.4}$$

where a is a positive constant, (A.3) is converted into

$$E' = \frac{j\omega\mu_0 J_s}{\pi} \int_\infty^{2/g'} \frac{1}{z^2} \sinh^{-1}\frac{z}{2/h'} dz. \tag{A.5}$$

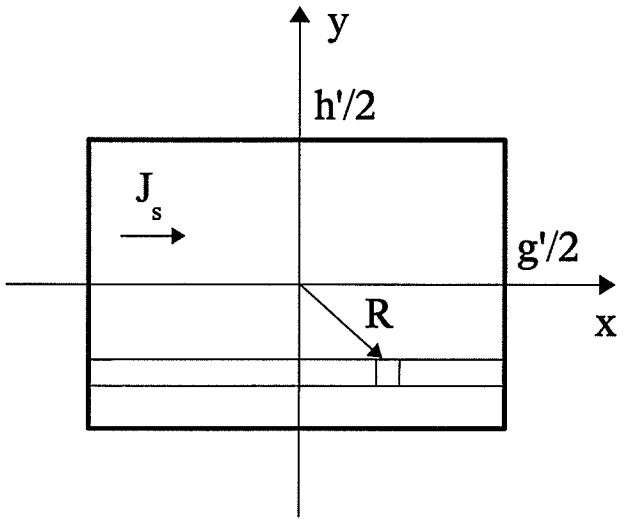

Figure A.1: Rectangular self-patch

The above integral is solved using formula 731.2 in [2]. The result is

$$E' = -\frac{j\omega\mu_0 J_s}{\pi}\left[\frac{1}{z}\sinh^{-1}\frac{zh'}{2} + \frac{h'}{2}\ln\left(\frac{2/h' + \sqrt{z^2 + (2/h')^2}}{z}\right)\right]_{\infty.}^{2/g'} \tag{A.6}$$

When $z \to \infty$, $\ln\left(\frac{2/h'+\sqrt{z^2+(2/h')^2}}{z}\right) \to 0$. Applying the l'Hopital rule, it can be shown that $1/z\sinh^{-1}(zh'/2) \to 0$ when $z \to \infty$. Then, E' is obtained in the form

$$\begin{aligned} E' &= -\frac{j\omega\mu_0 J_s}{\pi}\left[\frac{g'}{2}\sinh^{-1}\frac{h'}{g'} + \frac{h'}{2}\ln\left(\frac{2/h' + \sqrt{(2/g')^2 + (2/h')^2}}{2/g'}\right)\right] \\ &= -\frac{j\omega\mu_0 J_s}{2\pi}\left[g'\ln\left(\frac{h' + \sqrt{(h')^2 + (g')^2}}{g'}\right) + h'\ln\left(\frac{g'}{h'} + \sqrt{1 + \left(\frac{g'}{h'}\right)^2}\right)\right] \\ &= -\frac{j\omega\mu_0 J_s}{2\pi}\left[g'\ln\left(\frac{h'}{g'} + \sqrt{1 + \left(\frac{h'}{g'}\right)^2}\right) + h'\ln\left(\frac{g'}{h'} + \sqrt{1 + \left(\frac{g'}{h'}\right)^2}\right)\right]. \end{aligned} \tag{A.7}$$

Appendix B

Vector Products in Different Coordinate Systems

B.1 Spherical and Rectangular Coordinates

A position vector of a point P with rectangular coordinates (x,y,z) is given by $\boldsymbol{r} = x\boldsymbol{u}_x + y\boldsymbol{u}_y + z\boldsymbol{u}_z$. The unit vector $\boldsymbol{u}_\theta$ directed in the increasing sense of the spherical coordinate θ is expressed as

$$\boldsymbol{u}_\theta = \frac{1}{r}\frac{\partial \boldsymbol{r}}{\partial \theta} = \frac{1}{r}\left[\frac{\partial x}{\partial \theta}\boldsymbol{u}_x + \frac{\partial y}{\partial \theta}\boldsymbol{u}_y + \frac{\partial z}{\partial \theta}\boldsymbol{u}_z\right]. \tag{A.1}$$

Then

$$\boldsymbol{u}_\theta \cdot \boldsymbol{u}_x = \frac{1}{r}\frac{\partial r\sin\theta\cos\phi}{\partial\theta} = \cos\theta\cos\phi \tag{A.2}$$

$$\boldsymbol{u}_\theta \cdot \boldsymbol{u}_y = \frac{1}{r}\frac{\partial r\sin\theta\sin\phi}{\partial\theta} = \cos\theta\sin\phi \tag{A.3}$$

$$\boldsymbol{u}_\theta \cdot \boldsymbol{u}_z = \frac{1}{r}\frac{\partial r\cos\theta}{\partial\theta} = -\sin\theta \tag{A.4}$$

B.2 Prolate Spheroidal and Rectangular Coordinates

The relation between (x,y,z) and the prolate spheroidal coordinates (η,ξ,ϕ) has been given in chapter 5. The unit vector

$$\boldsymbol{u}_\eta = \frac{1}{h_\eta}\frac{\partial \boldsymbol{r}}{\partial \eta} = \frac{1}{h_\eta}\left[\frac{\partial x}{\partial \eta}\boldsymbol{u}_x + \frac{\partial y}{\partial \eta}\boldsymbol{u}_y + \frac{\partial z}{\partial \eta}\boldsymbol{u}_z\right] \tag{A.5}$$

where h_η is the Lamé parameter as described in chapter 5. For $\phi = 0$, we obtain

$$\boldsymbol{u}_\eta \cdot \boldsymbol{u}_x = \frac{1}{h_\eta}\frac{\partial x}{\partial \eta} = \frac{1}{h_\eta}\frac{\partial(c\sqrt{(1-\eta^2)(\xi^2-1)})}{\partial \eta} = -\eta\sqrt{\frac{\xi^2-1}{\xi^2-\eta^2}} \tag{A.6}$$

$$\boldsymbol{u}_\eta \cdot \boldsymbol{u}_y = \frac{1}{h_\eta}\frac{\partial y}{\partial \eta} = 0 \tag{A.7}$$

$$\boldsymbol{u}_\eta \cdot \boldsymbol{u}_z = \frac{1}{h_\eta}\frac{\partial z}{\partial \eta} = \frac{1}{h_\eta}\frac{\partial(c\eta\xi)}{\partial \eta} = \xi\sqrt{\frac{1-\eta^2}{\xi^2-\eta^2}} \tag{A.8}$$

B.3 Oblate Spheroidal Coordinates and Rectangular Coordinates

The η-directed unit vector in oblate spheroidal coordinate (η, ξ, ϕ) is

$$\boldsymbol{u}_\eta = \frac{1}{h_\eta}\frac{\partial \boldsymbol{r}}{\partial \eta} = \frac{1}{h_\eta}\left[\frac{\partial x}{\partial \eta}\boldsymbol{u}_x + \frac{\partial y}{\partial \eta}\boldsymbol{u}_y + \frac{\partial z}{\partial \eta}\boldsymbol{u}_z\right] \tag{A.9}$$

where $h_\eta = c\sqrt{\xi^2+\eta^2}/\sqrt{1-\eta^2}$. The relationship between (x, y, z) and (η, ξ, ϕ) are given in Chapter 6. When $\phi = 0$, we have

$$\boldsymbol{u}_\eta \cdot \boldsymbol{u}_x = \frac{1}{h_\eta}\frac{\partial x}{\partial \eta} = \frac{1}{h_\eta}\frac{\partial(c\sqrt{(1-\eta^2)(\xi^2+1)})}{\partial \eta} = -\eta\sqrt{\frac{\xi^2+1}{\xi^2+\eta^2}} \tag{A.10}$$

$$\boldsymbol{u}_\eta \cdot \boldsymbol{u}_y = \frac{1}{h_\eta}\frac{\partial y}{\partial \eta} = 0 \tag{A.11}$$

$$\boldsymbol{u}_\eta \cdot \boldsymbol{u}_z = \frac{1}{h_\eta}\frac{\partial z}{\partial \eta} = \frac{1}{h_\eta}\frac{\partial(c\eta\xi)}{\partial \eta} = \xi\sqrt{\frac{1-\eta^2}{\xi^2+\eta^2}} \tag{A.12}$$

Bibliography

[1] I.R. Ciric, *Electromagnetc levitation in axially symmetric systems*, Rev. Roum. Sci. Techn.-Électrotechn. et Énerg. **15** (1970), 35–71.

[2] H. B. Dwight, *Tables of integrals and other mathamatical data*, fourth ed., Macmillan, Toronto, 1961.

[3] A. Gray, *Modern differential geometry of curves and surfaces with mathamatica*, second ed., F:LCRC Press, Boca Raton, 1997.

[4] R. F. Harrington, *Time harmonic electromagnetic fields*, first ed., McGraw-Hill, New York, 1961.

[5] ———, *Field computation by moment methods*, first ed., Macmillan, New York, 1968.

[6] Himal C. Jayatilaka and Ioan R. Ciric, *Performance of surface impedance integral equation for quasistationary field analysis in axisymmetric systems*, COMPUMAG New York (2003), 184–185.

[7] W. Jingguo and J.D. Lavers, *Modified surface impedance boundary conditions for 3d eddy current problems*, IEEE Transaction on magnetics **29** (1993), 1826–1829.

[8] A.W. Mane, *The formulation of a general diffraction problem by an integral equation*, Zeitschrift für physik (1949), 601–618.

[9] Mayergoyz and G. Bredosian, *On finite element implementation of impedance boundary conditions*, J. Appl. Phys. **75** (1994), 6027–6029.

[10] K.M. Mitzner, *An integral equation approach to scattering from a body of finite conductivity*, Radio Science **2** (1967), 1459–1470.

[11] C. Müller, *Foundation of the mathematical theory of electromagnetic waves*, Springer Velag, New York, 1969.

[12] J.H. Richmond, *Scattering by a dielectric cylinder of arbitrary cross section shape*, IEEE Trans. Antennas Propagat. **13** (1965), 334–341.

[13] W.R Smith, *Static and dynamic electricity*, second ed., McGraw-Hill, New York, 1950.

[14] O. Sterz and C. Schwab, *A scalar boundary integrodifferential equation for eddy current problems using an impedance boundary condition*, Comput. Visual Sci. **3** (2001), 209–217.

[15] J.A. Stratton, *Electromagnetics theory*, first ed., McGraw-Hill, New York, 1941.

[16] D. J. Struik, *Lectures on classical differential goemetry*, second ed., Addison-Wesley, Massachusetts, 1961.

[17] B.S. Thornton and W. Brisley, *Electromagnetic levitation calculations for axially symmetric systems*, BRJT. Appl. Phys. **14** (1963), 682–686.